Agulhas Ring Heat Content and Transport in the South Atlantic Estimated by Combining Satellite Altimetry and Argo Profiling Floats Data

R. Laxenaire, S. Speich, A. Stegner

JGR Oceans

RESEARCH ARTICLE
10.1029/2019JC015511

Key Points:
- Most of the Agulhas rings are subsurface intensified in the central South Atlantic Ocean
- New method for individual reconstruction of heat content anomalies in well-sampled eddies improves the assessment of eddy variability
- An estimate of about 0.02 PW of heat flux achieved by the Agulhas Ring across the central South Atlantic is provided

Supporting Information:
- Supporting Information S1
- Figure S1
- Figure S2
- Figure S3
- Figure S4
- Figure S5

Correspondence to:
R. Laxenaire,
rlaxenaire@fsu.edu

Citation:
Laxenaire, R., Speich, S., & Stegner, A. (2020). Agulhas ring heat content and transport in the South Atlantic estimated by combining satellite altimetry and Argo profiling floats data. *Journal of Geophysical Research: Oceans*, *125*, e2019JC015511. https://doi.org/10.1029/2019JC015511

Received 23 JUL 2019
Accepted 18 AUG 2020
Accepted article online 22 AUG 2020

Agulhas Ring Heat Content and Transport in the South Atlantic Estimated by Combining Satellite Altimetry and Argo Profiling Floats Data

R. Laxenaire[1,2], S. Speich[1], and A. Stegner[1]

[1]Laboratoire de Météorologie Dynamique, UMR 8539 École Polytechnique, ENS, CNRS, Paris, France, [2]Center for Ocean-Atmospheric Prediction Studies, Florida State University, Tallahassee, FL, USA

Abstract The Agulhas leakage of Indian Ocean waters into the Atlantic has been shown to be a key link in global ocean circulation and climate; an increased understanding of this process is therefore of more than just of local interest. While knowledge of the Agulhas leakage has increased over the past 30 years, the precise mechanisms at play and water properties transferred are still not sufficiently documented. This study covers the Agulhas rings heat content and transport, which contribute to the meridional overturning circulation of the global ocean during their route across the South Atlantic Ocean. By applying TOEddies, an eddy detection and tracking algorithm that takes into account eddy merging and splitting, to satellite altimetry maps combined with a colocation of the detected eddies with Argo floats vertical profiles, we are able to document the important heat anomaly characterizing Agulhas rings and their evolution across the Cape Basin and the South Atlantic Ocean. Notwithstanding that in situ data coverage is still limited at the ocean mesoscale, we have estimated an averaged Agulhas rings subsurface heat transport of 2.5×10^{-2} PW and 1.5×10^{-2} PW across the eastern and western South Atlantic Ocean, respectively.

Plain Language Summary Mesoscale eddies are ubiquitous structures in the ocean. By containing more than half of the kinetic energy of the ocean circulation, they clearly shape it. They are also suspected to play a crucial role in transporting and mixing heat, salt, chemicals, and other materials within and among ocean basins. Because of this, they are alleged to impact the Earth climate and its changes. This should be true, in particular, south of Africa where the largest mesoscales eddies, the so-called Agulhas rings, are shed from the Agulhas Current into the Cape Basin conveying Indian warm and salty waters into the southeast Atlantic Ocean. However, due to their small-scale and highly variable nature, ocean eddies are inadequately sampled and poorly reproduced in numerical models. By using an eddy atlas built on satellite altimetry and associated to subsurface in situ observations acquired by the Argo profiling floats international program, we present new estimate of the role of Agulhas rings in advecting large quantity of heat across the South Atlantic basin. The results of our study are crucial to improve the understanding and modeling of ocean dynamics and the Earth climate.

1. Introduction

Ocean dynamics are highly nonlinear and characterized by physical processes giving rise to features across a broad range of spatial scales, from 1,000 km down to 1 km and even smaller. Notable among these features are mesoscale eddies, which refer to coherent structures that generally have spatial scales of 20–200 km and time scales of 10–100 days (Carton, 2001; Chelton et al., 2011; Morrow & Le Traon, 2012). The energy of these mesoscale eddies, which are omnipresent in the upper ocean layers (Stammer, 1997), typically exceeds that of the larger- and smaller-scale flows by an order of magnitude or more. In particular, they are associated with a peak in the kinetic energy spectrum in the subinertial frequency band (for a review, see Ferrari & Wunsch, 2009). Mesoscale eddies impact all the different dynamical components of the ocean, from the air-sea fluxes (e.g., Frenger et al., 2013) to the ventilation of the oceans deep interior (Sallée et al., 2010) and large-scale ocean circulation (Morrow et al., 1994; Lozier, 1997). Moreover, they are believed to play a major role in the transport of heat, salt, carbon, and chemical components as they propagate in the ocean and therefore represent a key dynamical element in the global budgets of these tracers (Bryden, 1979; Jayne & Marotzke, 2002; Morrow & Le Traon, 2012; Wunsch, 1999).

With the advent of satellite altimetry, many studies over the last 25 years have been dedicated to the general assessment of upper-ocean mesoscale characteristics and propagation properties (e.g., Chelton et al., 2007, 2011; Chaigneau et al., 2008). However, over the last few years there has been increased interest specifically in the merging and splitting events associated with these eddies (e.g., Du et al., 2014; Laxenaire et al., 2018; Le Vu et al., 2018; Li et al., 2014; Yi et al., 2014). By accurately accounting for these events, such studies have revealed a more complex eddy dynamic than previously documented. Yet the description of these eddies from satellite altimetry maps is not complete, as only their surface signature can be characterized via satellite altimetry. For instance, it was shown by recent studies that surface- and subsurface-intensified eddies exhibit sea surface height (SSH) anomalies of the same sign but distinct sea surface temperature anomalies (Assassi et al., 2016) and vertical hydrographic structures (e.g., Chaigneau et al., 2011; Pegliasco et al., 2015; Zhang et al., 2017). This is of great importance as nicely reviewed by Ciani (2016), which, by detailing examples of subsurface-intensified eddies, showed that such structures can be found throughout the Ocean.

To further our knowledge of global ocean eddies, recent studies have attempted to systematically combine satellite altimetry observations of eddies with vertical profiles from Argo floats to provide three-dimensional eddy reconstructions (e.g., Chaigneau et al., 2011; Nencioli et al., 2018; Pegliasco et al., 2015; Souza et al., 2011; Yang et al., 2013). Those efforts have confirmed that mesoscale eddies can advect large amounts of water, heat, and salt by trapping and transporting water masses within their core as they propagate. However, it is complicated to obtain an accurate estimate of their properties and to generalize for the same family of eddies (i.e., of the same polarity, generated in the same region). Indeed, in situ data coverage is still sparse at the ocean mesoscale, despite much improvement in the last 15 years with the advent and development of the Argo profiling floats international program.

In particular, previous studies have tried to estimate the properties and transport of eddies using in situ and satellite altimetry in two ways. The first and most widely used approach is the composite method, which is based on the computation of eddy composites within box areas (e.g., Chaigneau et al., 2011; de Marez et al., 2019; Yang et al., 2013). This method relies on the hypothesis that eddies of the same polarity in a given geographical area have similar hydrographic properties. The second approach involves individual reconstruction of one or more eddies sufficiently sampled by in situ observations along their trajectories and attempting to generalize the results by assuming that eddy properties and trajectories were representative of a specific family of eddies in a given region (e.g., Ballegooyen et al., 1994; Duncombe Rae et al., 1996; Nencioli et al., 2018; Souza et al., 2011). This approach gains in robustness with the number of eddies it reconstructs. However, a family of eddies can display a relatively broad diversity of properties and this needs to be accounted for.

Using one of these two approaches, it is possible to estimate the transport of volume, heat, and salt by the eddies by combining their hydrographic properties with the eddy trajectories derived from satellite altimetry (Souza et al., 2011; Laxenaire et al., 2019; Nencioli et al., 2018). The transport of water masses and heat by mesoscale eddies is particularly important for large eddies such as the Agulhas rings (Lutjeharms, 2006). Agulhas rings are anticyclonic eddies shed from the Agulhas Current, the western boundary current of the south Indian Ocean, at its retroflection south of Africa (Bang, 1970; Duncombe Rae, 1991; Lutjeharms & Gordon, 1987; Gordon & Haxby, 1990; Olson & Evans, 1986).

These eddies are thought to account for an important fraction of the so-called Agulhas Leakage (De Ruijter et al., 1999; Lutjeharms, 2006). The Agulhas Leakage is a relatively substantial transfer (about 15 Sv) of southwest Indian Ocean thermocline water into the South Atlantic via the Cape Basin (a basin lying at the southwestern tip of Africa) (Arhan et al., 1999, 2011; Ballegooyen et al., 1994; Garzoli et al., 1999). The Agulhas Leakage has been shown to impact the regional climate of South Africa (Cheng et al., 2018; Walker, 1990; Walker & Mey, 1988) as well the climate at a global scale by substantially influencing the Atlantic Meridional Overturning Circulation (AMOC) advecting warm and saline waters (Beal et al., 2011; Biastoch et al., 2009; Donners & Drijfhout, 2004; Dong et al., 2011; Gordon et al., 1992; Lampitt et al., 2010). However, despite many advances in the assessment of mesoscale eddies and of Agulhas rings in particular, an adequate quantitative characterization of their three-dimensional subsurface-intensified structure, the phenomenological understanding of their role in the global ocean circulation, and the properties they transport (heat, salt, and biogeochemical variables) is still essentially undocumented.

This can be linked to the variety of Agulhas rings hyrographic structure observed. For instance, Arhan et al. (1999) and Garzoli et al. (1999) described subsurface anticyclonic eddies in the Cape Basin and in the eastern part of the Atlantic Ocean. These authors qualified the features as "modified Agulhas rings" that were propagating as subsurface eddies, without being in contact with the atmosphere. Herbette et al. (2004) showed numerically that this type of eddy could evolve from surface- to subsurface-intensified vortices via lateral advection subducting below lighter waters. In a recent study, Laxenaire et al. (2019) achieved a Lagrangian reconstruction of an Agulhas ring by colocating the eddy contour with subsurface observations derived by Argo profiling floats. In that work, Laxenaire et al. (2019) provided evidence of the en route modification of that Agulhas ring. In particular, the Agulhas ring transitioned from a surface- to a subsurface-intensified eddy. In spite of that eddy sank into depth, it was still associated to a sea surface signature. Comparing the upper layers temperature-salinity properties in the Agulhas ring with those of the environment, the authors showed that the Agulhas ring contains modified water close to the surface, which would indicate a subduction due to the restratification of the Agulhas ring. In the same study, Laxenaire et al. (2019) qualitatively identified from historical observations the horizontal shape of the pycnocline above the hydrographic core of those Agulhas rings referenced in the literature. They flagged subsurface-intensified eddies as those showing a doming of isopycnals in their upper layers. This comparison qualitatively supports the existence of both surface- and subsurface-intensified Agulhas rings in the South Atlantic Ocean.

In this work, we explore and discuss Agulhas ring properties inferred with the TOEddies eddy detection method applied to 18 years (from 2000 to 2017) of altimetry ADT maps colocated with more than 2,000 hydrographic profiles from the Argo profiling floats program. This complex network of Agulhas ring trajectories is explored to provide a relatively precise assessment of the vertical extension of Agulhas rings that needs to be taken into account in order to correctly evaluate their heat content (HC). We then provide estimates of Agulhas ring HC anomalies comparing individual reconstruction of Agulhas ring segments and eddy-composite methods. Finally, we conclude the study with an assessment of subsurface heat transport associated with Agulhas rings.

This manuscript is organized as follows. In section 2, we introduce the data and the method used to define Agulhas ring trajectories and their colocation with Argo vertical profiles. In section 3, we present the results of this study starting with the characterization of surface and subsurface Agulhas rings following as well as the determination of the depth levels needed to correctly estimate the heat anomalies associated with Agulhas rings. Then we focus on the assessment of the Agulhas ring HC and associated heat transport. These results and their limitations are then discussed in section 4 before summarizing our new findings and major conclusions in section 5.

2. Materials and Methods

2.1. Eddy Detection and the AR Eddy Network

Under the geostrophic approximation, closed contours of SSH correspond to closed stream functions that can be used to identify geostrophic eddies. This property has enabled the identification and tracking of mesoscale eddies from gridded altimetric maps first made available in the 1990s (for an up-to-date review, we refer readers to Chapter 10 of Stammer & Cazenave, 2017). The availability of these maps has allowed the development of systematic eddy detection and the derivation of their trajectories via the development of various algorithms (e.g., Ashkezari et al., 2016; Chaigneau et al., 2011; Chelton et al., 2011; Doglioli et al., 2007; Faghmous et al., 2015; Isern-Fontanet et al., 2006; Laxenaire et al., 2018; Le Vu et al., 2018; Mason et al., 2014; Matsuoka et al., 2016; Nencioli et al., 2010; Pegliasco et al., 2015; Qiu-Yang et al., 2016).

However, most of the previous approaches do not take into account the fact that mesoscale eddies display complex behavior and often experience episodes during which they split into two or more mesoscale structures or merge with neighboring eddies. This is particularly true for Agulhas rings, as evidenced by both in situ and remote sensing studies (Arhan et al., 1999; Baker-Yeboah et al., 2010; Boebel et al., 2003; Byrne et al., 1995; Dencausse et al., 2010b). With the aims to understand such processes, various studies developed algorithms able to identify and record splitting and merging of eddies (e.g., Cui et al., 2019; Le Vu et al., 2018; Pegliasco et al., 2015). The TOEddies method is based on the eddy-tracking method developed by Chaigneau et al. (2011) that was subsequently improved by Pegliasco et al. (2015) and Laxenaire et al. (2018). TOEddies identifies eddies as closed-contour ADT in daily altimetry maps (Duacs/AVISO+, 2015) and uses the

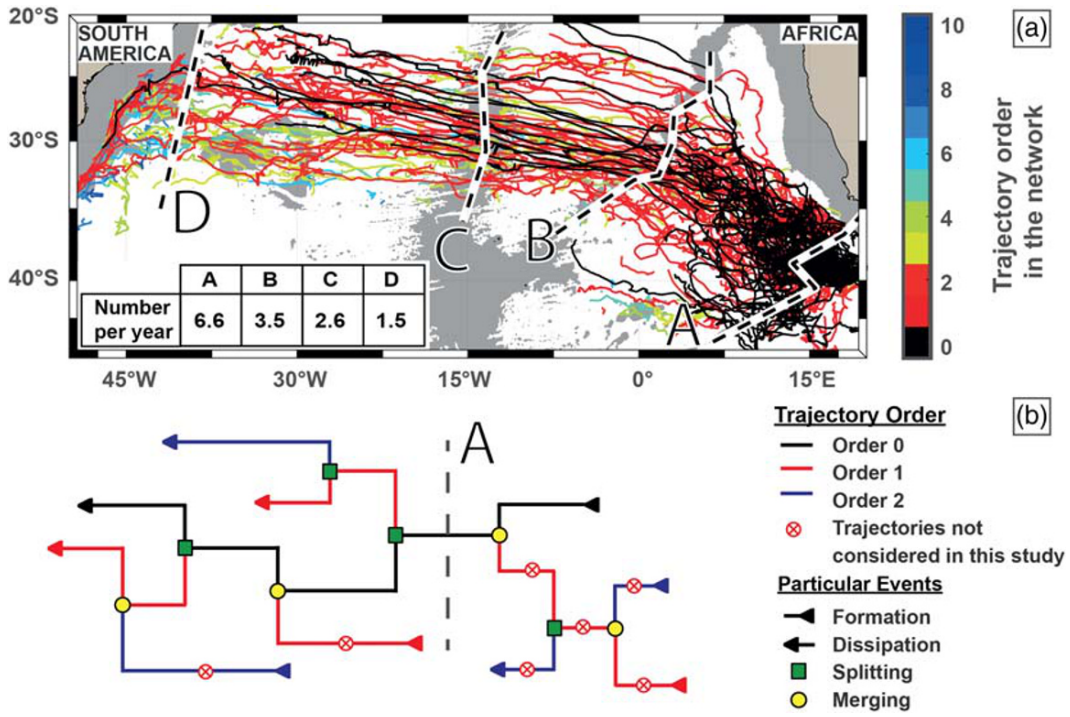

Figure 1. (a) Agulhas ring (AR) trajectories defined as Agulhas ring eddy network (AREN) trajectories that can be tracked back to the Agulhas retroflection. The black color is for Order 0 (AR-0), which we defined as the Agulhas ring main trajectories, and higher order indicates the number of splitting event needed to tack back any trajectory to an AR-0. Five sections (A to D) were used to derive the number of AR trajectories crossing per year during the period January 2000 to December 2017. The gray shading in each panel represents water depths of less than 3,500 m in the ETOPO1 data set (Amante & Eakins, 2009). Note that Sections A to C follow bathymetric features. (b) Schematic of the reconstructed AR from the complete AREN where the segments that do not participate in interocean exchanges, and thus are out of the scope of this study, are indicated by red crosses.

superposition of the areas occupied by one eddy on two consecutive days to reconstruct its trajectory. In eddy merging and splitting events, the area of one vortex overlaps with the area of more than one structure. In these cases, a cost function is used to identify the main trajectories. We refer to the section 2.2 of Laxenaire et al. (2018) for a complete description of this algorithm and its validation using the independent looping surface drifters data set provided by Lumpkin (2016) and compared to the AVISO eddy database (Duacs/AVISO+, 2017).

This study uses the TOEddies algorithm to identify and track eddies across 24 years of ADT data (from January 1993 to June 2018) within the South Atlantic [70°W to 65°E; 55–15°S] (see Figure 1a). The result database of eddies and eddy trajectories contains only cyclonic and anticyclonic trajectories lasting for at least four weeks. While the total surface of one eddy is limited by the farthest ADT closed contour containing its center, we define the eddy's dynamical core (or characteristic core) as the area encompassed by the closed contour associated with the maximum azimuthal geostrophic velocities derived from ADT maps (Duacs/AVISO+, 2015). The area of this characteristic core (A_{Vmax}) is used to define an equivalent radius (R_{Vmax}) as $R_{\mathrm{Vmax}} = \sqrt{A_{\mathrm{Vmax}}/\pi}$ as well as the eddy center corresponding to the centroid of this area. A similar equivalent radius (R_{Out}) is defined for the outermost closed contour of the eddy.

Following the definition of Laxenaire et al. (2018), we identify Agulhas ring main trajectories as the anticyclonic eddies that enter the Cape Basin by crossing its southeastern limit, illustrated by the A-line in Figure 1a. While their shedding is not directly identified, this definition restricts their first detection to an area very close to the retroflection and allows us to classify Agulhas rings as those anticyclonic eddies most likely containing Indian Ocean water originating from the Agulhas Current and then entering the South Atlantic. There, they can span very long distances and can have a lifetime of several years (e.g., Byrne

et al., 1995). To ensure the consistency of the recovered trajectories, we only use the trajectories reconstructed for the period January 2000 to December 2017.

To recover the whole set of trajectories linked with Agulhas rings, we included the anticyclonic trajectories that interact with the Agulhas rings by reconstructing an eddy network linking trajectories together. Each trajectory in this Agulhas ring eddy network (AREN) (Laxenaire et al., 2018) is associated to an order being determined by flagging the number of eddy splittings and mergings needing to be taken into account to link a specific trajectory to an Agulhas ring main trajectory that corresponds to the Order 0. Details on how AREN trajectories are computed can be found in Laxenaire et al. (2018) and a schematic is provided in Figure 1b. Given that the aim of the present study is the assessment of the HC and transport achieved by Agulhas rings, in the following we only take into account the Agulhas ring main trajectories (Order 0 AREN set) and those higher-order ARENs whose trajectories participate in the interocean exchange. Therefore, we only consider here the set of higher-order AREN segments that are stem from splitting of Agulhas rings in the Atlantic Ocean. By following the definition of Agulhas ring we adopted, the selected AREN correspond to Agulhas ring water only as they can be tracked back to the Agulhas retroflection. We will thus refer to them as ARs, and, in this case, the order accounts for the number of splitting events needed to be taken into account to link a specific trajectory to an Order 0 AR. Of the ARs detected, 127 are Order 0 AR trajectories and 523 are higher order. In the following, the order from the AR analysis is added to indicate the type of AR when necessary.

2.2. Argo Profiles Data and Eddy Colocation

Argo floats provide a large number of CTD (conductivity, temperature, and depth) vertical profiles for the upper 2,000 m of the global ocean. These data are collected and made freely available by the International Argo Program and the national programs that contribute to it (doi:<http://doi.org/10.17882/42182>) as part of the Global Ocean Observing System. Argo data centers provide delayed mode data for each vertical profile. This mode corresponds to validated and calibrated profiles by the delayed-mode operators (e.g., Cabanes et al., 2016; Owens & Wong, 2009), where errors associated with pressure are corrected based on the surface pressure recorded by the float and salinity sensor drift are corrected against the most up-to-date global climatology (computed with both full-depth CTD from oceanographic research cruises and validated Argo floats).

In this study, we use the delayed mode Argo data available at the Coriolis Global Data Center (Coriolis GDAC; url:<http://www.coriolis.eu.org>) with quality-control flags equal to 1 and 2 (which refers to good observation and probably good observation respectively). According to the GDACs, the accuracy in the resulting profiles are ± 0.002°C for the in situ temperatures (T), ± 2.4 dbar for the pressures, and below ± 0.01 psu for the practical salinities (S_P). We retain on profiles containing at least one observation in the upper 20 m and one at a depth greater than 1,200 m. Within these profiles and following Chaigneau et al. (2011), we then select those profiles with a minimum vertical resolution within 25, 50, 75, 100, and 200 m for, respectively, the depth intervals 0–100 m, 100–300 m, 300–500 m, 500–1,000 m, and below 1,000 m. The data for the profiles satisfying all these criteria are interpolated vertically at a 10-m depth step. Selected CTD profiles are then converted into conservative temperature (Θ), absolute salinity (S_A), and potential density anomaly (σ_0) profiles using the Gibbs SeaWater (GSW) Oceanographic Toolbox of the Thermodynamic Equation of SeaWater 2010 (TEOS-10) (McDougall & Barker, 2011). Finally, the anomalies of these variables are obtained by subtracting a local climatological profile computed from the newly released World Ocean Atlas 2018 (WOA18). For this purpose, the $1° \times 1°$ monthly climatology (Locarnini et al., 2019; Zweng et al., 2019) based on more than 10 years (2005–2017) of observations is used. Hydrographic fields are converted into Θ, S_A, and σ_0 using the GSW Oceanographic Toolbox (McDougall & Barker, 2011). These fields are linearly interpolated at the position and day of the year of each profiling float (we assume that the WOA18 monthly climatology represents the ocean state of the middle of the month). Finally, an estimation of the accuracy on the Argo profiles and associated anomalies is computed as detailed in Appendix A1. It results into uncertainties of about 0.07 g kg^{-1} (0.1 g kg^{-1}) for S_A, 0.02°C (0.1°C) for Θ, and about 0.05 kg m^{-3} (0.1 kg m^{-3}) for σ_0 for the observations (anomalies) of the hydrographic profiles.

The selected Argo profiles are colocated with the mesoscale eddies contained in the TOEddies database revealing 2,095 profiles within the South Atlantic that lie within ARs. The distribution of these profiles as a function of the order of ARs is presented in Figure 2a. It shows that around half of the profiles (48%) lie

within Order 0 ARs. For ARs of Orders 0 to 2, the percentage of Argo profiles captured within one of these eddies increases to 94%. It is important here to note that the colocation accuracy of the Argo profiles with mesoscale eddies is both impacted by the accuracy of the eddy center determination and the exact surfacing position of Argo profiles. Lebedev et al. (2007) and Chaigneau et al. (2011), by taking into account the surface drift of the Argo profiles before the determination of their position, estimated an average error of Argo position smaller than 1 km. This number is small when compared to the (1/4)° × (1/4)° horizontal resolution of the altimetric maps (i.e., 10–20 km in the area of interest) that we expect to have a major impact on the correct center determination. For example, by shifting individual profiles to hydrographic properties of a reconstructed ARs identified with TOEddies, Laxenaire et al. (2019) estimated a mean error of 16 km on the distance from the center. This might result in the main source of uncertainties due to large horizontal gradient of hydrographic properties associated to mesoscale eddies and especially ARs. The histogram of the distance between each profile and the eddy center is presented in Figure 2b. It shows that less than 3% of the Argo profiles lie within a distance of 20 km from the eddy center. This value reaches 20% and 45% when the distance from the center is 50 and 80 km, respectively. These results suggest that Argo floats sample the outer area better than the inner core of the eddies, as already discussed by Chaigneau and Pizarro (2005) and Pegliasco et al. (2015). However, our statistics show that about half of the profiles (52%) fall within the eddy dynamical core delimited by the maximum of azimuthal velocities, R_{Vmax}, depicted by the darker bars in Figure 2.

Among all ARs identified from ADT maps, 204 (31%) were sampled at least once by an Argo profile. This number decreases dramatically when considering ARs sampled by more than one profile. Indeed, only 82, 30, and 6 ARs are sampled by 5, 20, and 40 profiles, respectively. Moreover, these profiles are not necessarily close in time and space as ARs can have a lifetime of several years (e.g., Byrne et al., 1995).

3. Hydrographic Properties of ARs

Here we use the total data set of Argo profiles colocated within ARs to assess their hydrographic properties via a semi-Eulerian framework. We use this terminology because eddies are studied regionally but their selection is achieved by identifying and tracking their trajectories using a Lagrangian approach. First, the hydrographic properties of eddies sampled by an Argo profile in the first half of the characteristic contour are examined to classify them as surface or subsurface intensified and to identify the depth interval of their maxima heat anomalies. Then, the obtained information is combined to estimate the HC anomalies associated with the AR in different regions using both composite and individual reconstructions.

3.1. Surface- Versus Subsurface-Intensified Eddies

In the first stage of this study, Argo profiles are analyzed independently to highlight the properties of the ARs sampled in the region of interest before any 3-D reconstruction. The magnitude of hydrographic properties, such as density anomalies (σ_0'), is expected to be larger for profiles lying close to the eddy center. Consequently, only the profiles surfacing at a distance from the eddy center less than half the R_{Vmax} are studied. This selection results into the identification of 252 Argo profiles with an average distance from the center of 30 km (less than 50 km for 85% of them). Taking a mean positioning error of 16 km (i.e., close to half of the averaged distance from the center), it ensures that profiles are in the eddy characteristic core.

The surface properties of the ocean are influenced by the atmospheric dynamic. Their uncertainties in measured water properties (including in derived climatologies such as the World Ocean Atlas [WOA18]) are larger than at depth. Consequently, we studied only the eddy properties below 100 m. This to ensure to be at depths larger than the mixed layer (ML) in most of the cases (e.g., Gaube et al., 2018) while capturing a large fraction of ARs, which are known to have a large vertical extension (e.g., Arhan et al., 1999). However, to be consistent, the mixed layer depth (MLD) is also computed from density profiles using the hybrid method developed by Holte and Talley (2009). When applied to Argo profiles (Holte et al., 2017), this method has proved to be more accurate than the one developed by de Boyer Montégut et al. (2004). The MLD in the 252 Argo profiles is shown in Figure 3. Only 26% of the profiles have a MLD deeper than 100 m. Thus, to ensure the robustness of our results the 100 m of each Argo profile, or the MLD if it is deeper, are not analyzed at this stage.

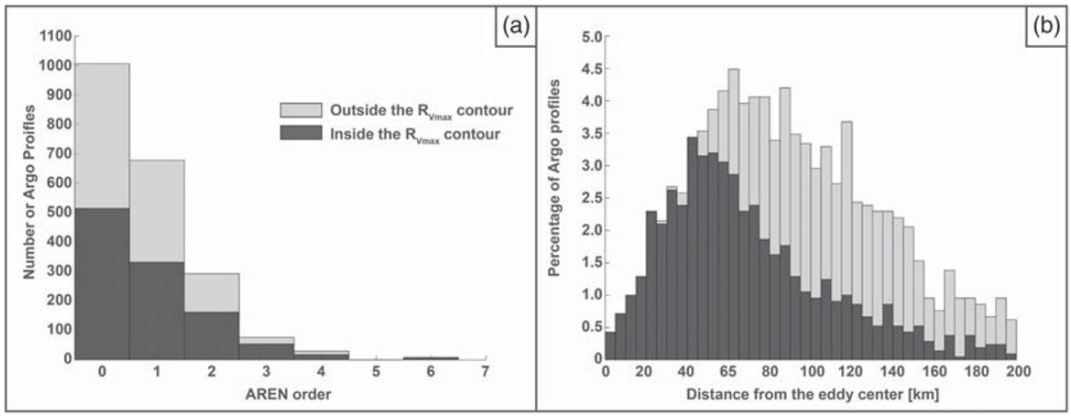

Figure 2. Histogram showing the number of Argo profiles sampling inside an Agulhas ring according to (a) the AR order and (b) the distance of the profiles position from the eddy center. A dark gray bar indicates that the Argo profile lies within the eddy core; otherwise the bar is shaded light gray.

ARs are large anticyclonic eddies associated to large positive temperature anomalies in their core (e.g., Arhan et al., 1999) and thus negative anomalies of density. To characterize the intensity of their hydrographic core, the min(σ_0') of each Argo profile below either the MLD or 100 m, whichever is deeper, is identified. In the previous section, we estimated an uncertainties on $|\sigma_0'|$ of 0.1 kg m^{-3}; thus, the profiles with σ_0' larger than −0.1 kg m^{-3} everywhere are flagged as suspicious as their anomalies are not significantly large. These suspicious profiles (black asterisks in Figure 3) account for 8% of the 252 selected Argo profiles. For a comparison, the same method is applied on Argo profiles sampling the first half of the characteristic core of an anticyclonic eddies detected by TOEddies that are not identified as ARs. Among these 1,317 profiles, 57% are flagged as suspicious. This indicates that the 0.1 kg m^{-3} uncertainty is relevant to the analysis of ARs known to be associated with particularly high hydrographic anomalies but would need to be relaxed to study weaker eddies.

At this step, a depth interval above the strongest subsurface density anomaly and below the MLD or 100 m, whichever is deeper, was identified in the 232 Argo profiles associated to significant min(σ_0'). The analysis of these subsurface layers allows to separate surface- and subsurface-intensified eddies as they are characterized by different vertical structures (e.g., Assassi et al., 2016; Chaigneau et al., 2011; Pegliasco et al., 2015;

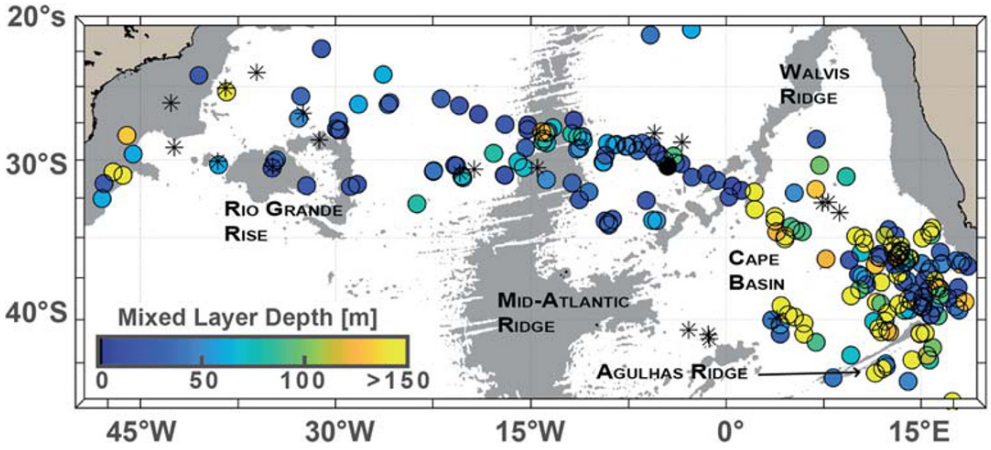

Figure 3. Mixed layer depth in the Agulhas rings. Only Argo profiles sampling inside an ARs at a distance from the center of less than half of its instantaneous R_{Vmax} are considered. Argo profiles associated to nonsignificant density anomalies (σ_0') (i.e., min(σ_0') ≥ −0.1 kg m^{-3}) are indicated by black asterisks. The gray shading in each panel represents water depths of less than 3,500 m in the ETOPO1 data set (Amante & Eakins, 2009).

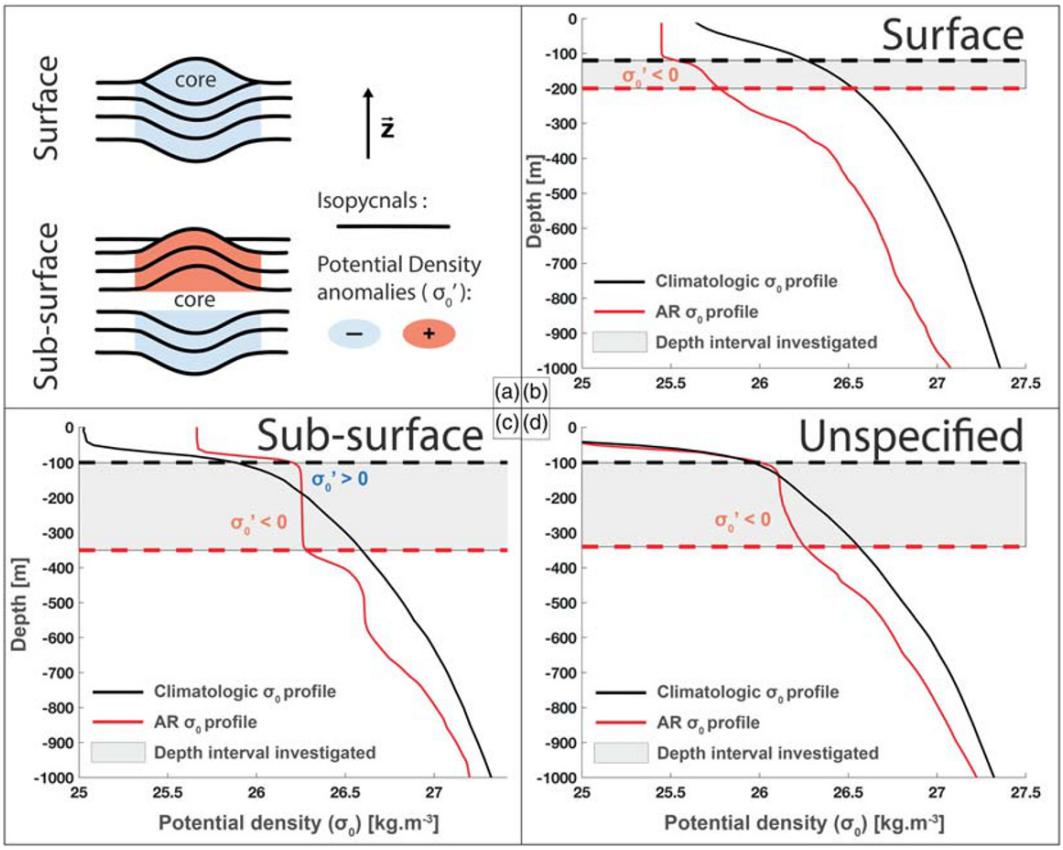

Figure 4. Schematic of isopycnal displacements and potential density anomaly for (a) surface- and subsurface-intensified anticyclonic eddies modified from Assassi et al. (2016). Example of (b) a surface-, (c) a subsurface-intensified eddies, and (d) one unspecified as identified from three Argo profiles sampling inside their core between 24 and 28 km from the center. The surface eddy is sampled the 10 March 2006 in the Cape Basin and both the subsurface one the 7 March 2013 and the unspecified one the 24 April 2015 are sampled between the Walvis Ridge and the Mid-Atlantic Ridge.

Zhang et al., 2017). The different situations considered in this study are schematized in Figure 4a modified from Figure 2 in Assassi et al. (2016). The simplest case is the surface-intensified anticyclonic eddies characterized by deepening of isopycnals and thus $\sigma_0' \leq 0$, from the surface to, at least, the position of it highest

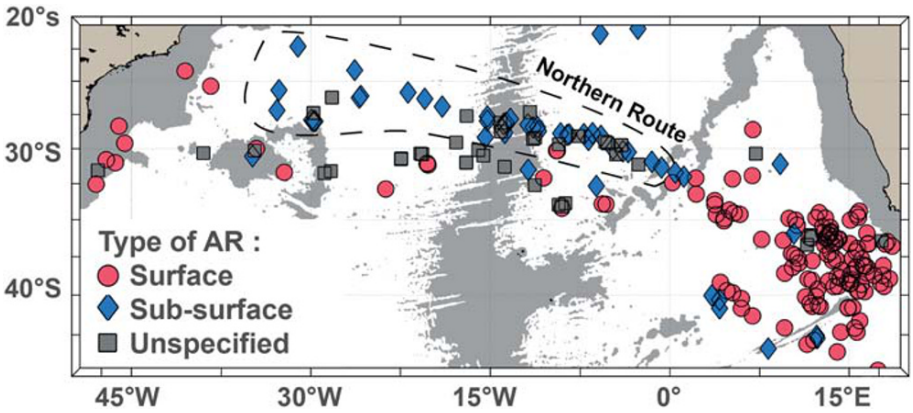

Figure 5. Type of anticyclonic eddies (surface-, subsurface-intensified, and unspecified) for Agulhas rings identified in the region. Only Argo profiles sampling inside an anticyclone at a distance from the center of less than half of its instantaneous R_{Vmax} are considered. The northern route is indicated by a dashed contours, and the southern route considered in the text corresponds to the profiles in the South Atlantic Ocean south of the northern one. The gray shading in each panel represents water depths of less than 3,500 m in the ETOPO1 data set (Amante & Eakins, 2009).

density anomaly. On the other hand, the typical subsurface-intensified anticyclones are lens shaped (e.g., McWilliams, 1985; McGillicuddy et al., 1999; Nan et al., 2017; Sánchez & Gil, 2004; Stammer et al., 1991; Sweeney et al., 2003; Wang et al., 2019) and are thus characterized by a deepening (dooming) of isopycnals below (above) their hydrographic core. Such a different shape of the isopycnals leads to the superposition of layers of σ_0' with different signs: negative below the core, 0 at its level, and positive above it. As discussed in Assassi et al. (2016), this schematized picture does not change if a ML lies above the subsurface anticyclone. Consequently, the change of σ_0' between the min(σ_0') and the MLD can be used to identify subsurface anticyclonic eddies. By taking the estimated uncertainty for σ_0' into account, three different cases are defined of which an example of each is presented in Figures 4b–4d. Eddies sampled by Argo profiles where $\sigma_0' \leq -0.1\,\mathrm{kg\,m^{-3}}$ at every levels in the depth interval studied (e.g., Figure 4b) are identified as surface-intensified ARs. Subsurface-intensified ARs are those showing a change of σ_0' reaching, at least at one depth, $\sigma_0' \geq 0.1\,\mathrm{kg\,m^{-3}}$ in the interval (e.g., Figure 4c). Finally, those verifying $\sigma_0' \geq -0.1\,\mathrm{kg\,m^{-3}}$ but not $\sigma_0' \geq 0.1\,\mathrm{kg\,m^{-3}}$ are characterized as "unspecified" (e.g., Figure 4d). It is worth noting that 83% of the unspecified profiles show a $\sigma_0' \geq 0\,\mathrm{kg\,m^{-3}}$ within the studied interval of depth. This suggests that they might be subsurface-intensified ARs if uncertainties were not taken into account.

The 232 Argo profiles classified according to the three categories are presented in Figure 5. In Figures 3 and 5, two main regions stand out for ARs: (1) the Cape Basin, where surface-intensified eddies with a deep MLD prevail in 90% of the structures, and (2) the South Atlantic Ocean (i.e., between Segments B and D shown in Figure 1a), where subsurface-intensified eddies with a shallower MLD prevail in 47% of the structures whereas the undermined ones account for 39% of them. The transition seems to occur near the Walvis Ridge where both type of structure are visible.

ARs seem to follow two routes while crossing the South Atlantic Ocean: a northern route (Figure 5) and a southern route. Nearly all ARs following the northern route are subsurface eddies, whereas the three categories of ARs are found along the southern route. ARs reaching the western boundary along the eastern South American Margin become surface-intensified eddies independently of the route followed. To examine if this geographical distribution of surface- and subsurface-intensified eddies is specific to ARs, the same method is applied to the detected anticyclonic eddies that are not identified as ARs. The resulting map in the upper panel of Figure S1 in the supporting information does not show any clear pattern: Surface-intensified eddies (≥60%) and undermined ones (30%) populate most of the different areas of the region, while only 5% of them are subsurface in the Cape Basin and 8% in the South Atlantic Ocean.

3.2. Spatial Distribution of AR HC Anomaly

To estimate the HC and transport achieved by ARs, we first need to assess their HC anomaly. To do this, we compute the HC for both Argo profiles falling within ARs and local climatological profiles computed from WOA18, following Equation 1:

$$HC_{z_{low}}^{z_{up}}(r) = \int_{z_{low}}^{z_{up}} \rho(r, z) C_p \Theta(r, z) dz, \tag{1}$$

where C_p is the heat capacity (J/[kg K]), $\rho(r, z)$ the density ($\mathrm{kg\,m^{-3}}$), $\Theta(r, z)$ the conservative temperature (K), and z the depth (m) where up and low refer to upper and lower limits of the integration. The $HC(r)$ computed is not the total HC of the eddy but rather the vertically integrated one estimated at a fixed distance (r) from the center of the eddy. The heat content anomaly (HCA) is then obtained by subtracting the local climatological HC from the $HC(r)$ computed in the eddy.

As discussed in the previous section, ARs can be either surface- or subsurface-intensified eddies. In the reconstruction of such structures by Nencioli et al. (2018) and Laxenaire et al. (2019), the authors limited their analyses to the subsurface portion of the eddies, namely, below a depth of about 200 m. Indeed, at shallower depths, eddy properties were observed to vary at seasonal and higher frequency, while below 200 m they proved to be more coherent with time. Indeed, the depth of 200 m seems to lie below the regional seasonal thermocline, as suggested by the seasonal MLD maps produced by de Boyer Montégut et al. (2004) and the MLD computed within ARs as shown in Figure 3. It is comforted by individual inspections of the 65 profiles sampling a subsurface-intensified ARs identified in the previous section. The depth of the 200 m lies inside their homogeneous cores, which ensures that water masses below are not be impacted by surface

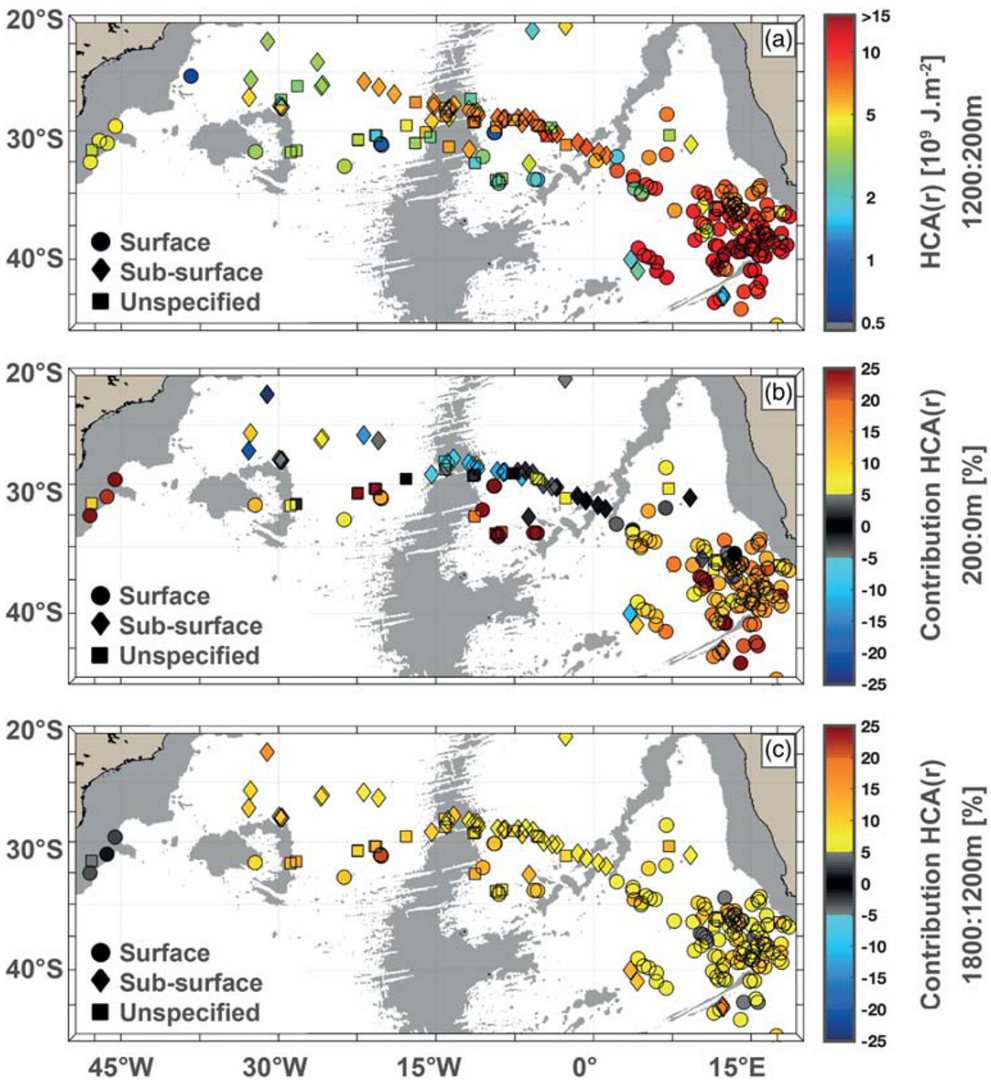

Figure 6. (a) Heat content anomalies (HCAs) for the profiles sampling inside an Agulhas ring (AR) integrated at a depth of 1,200 to 200 m ($HCA_{1200}^{200}(r)$). (b) Contribution to HCA for the upper 200-m layer ($ContribHCA(r)_{200}^{0}$) expressed as percentage of the total HCA following Equation 2. (c) Contribution to HCA for the 1,800- to 1,200-m layer ($ContribHCA(r)_{1800}^{1200}$) expressed as percentage of the total HCA following Equation 2. Contribution estimates (b and c) cannot be computed in Argo profiles not sampling 1,800 m and below. Argo profiles sampling inside a surface (subsurface) AR are indicated by a circle (diamond) marker in each panel. Those where the difference could not be determined are indicated by square marker. Only Argo profiles sampling inside an anticyclone at a distance from the center of less than half of its instantaneous R_{Vmax} are considered. The gray shading in each panel represents water depths of less than 3,500 m in the ETOPO1 data set (Amante & Eakins, 2009).

processes. Consequently, we prescribe the upper limit of the vertical integration of $HC(r)$ at 200 m ($z_{up} = 200$ m). We also fixed 1,200 m ($z_{low} = 1{,}200$ m) as the lower limit for the HC integration (corresponding to the profiling depth minimum we prescribed when selecting Argo profiles) in order to maximize the number of Argo profiles available without the need to extrapolate data below the deepest measurement. It is worth noting here that AR property anomalies are computed relative to their local climatological profile. Thus, as the hydrographic properties of the environment vary from area to area of the larger domain (in supporting information Figure S2), a direct comparison of HCA between remote regions can only be made with caution. This limitation was discussed in their supporting information by Souza et al. (2011) when computing their local temperature anomalies instead of a fixed pure South Atlantic Ocean water as

was done by Schmid et al. (2003). Souza et al. (2011) pointed out that an artificial bias is added in the anomalies due to the variation of the environment along the AR paths.

To estimate uncertainties on the HCA, we use the vertically averaged mean uncertainty estimated previously for Argo and the local climatological profiles. By using these averages, we consider that uncertainties on Θ and ρ are not correlated, which is not the case. However, following the law of propagation of independent uncertainty (BIPM, 2008) , it is possible to estimate the relative uncertainties of HC in the 1,200–200 interval by normalizing the uncertainties of 0.1 kg m^{-3} for ρ and 0.02 K for Θ by, respectively, 1,026 kg m^{-3} and 277 K, which are the lowest values of these quantities in the reconstructed AR by Laxenaire et al. (2019). Adding these relative uncertainties and converting them into absolute uncertainties using the $1{,}026 \times 10^9$ J m^{-2}, which is the maximum value of HC in the area of study (see Figure S2 in the supporting information), we obtain an estimation of the uncertainty for HC equal to 0.2×10^9 J m^{-2}. Using the same procedure for HC computed from the local climatological profiles, the total uncertainty for HCAs in the 200- to 1,200-m-depth interval amounts to 0.5×10^9 J m^{-2} is obtained.

Finally, as the temperature anomalies decrease rapidly far from the eddy center (e.g., Souza et al., 2011), we reiterate the procedure of the previous section selecting only Argo profiles sampling ARs at a distance of less than half the instantaneous value of R_{Vmax} and being associated to significant σ_0. However, here, the anomalies have to be computed at least down to 1,200 m, and some of the climatological profiles are not available for this depth because of the presence of bathymetric feature. The $HCA_{1200}^{200}(r)$ computed for the 221 Argo profiles is presented in Figure 6a. It shows that all surface-intensified eddies in the southeastern corner of the Cape Basin (and therefore close to the Agulhas Current retroflection) have high $HCA_{1200}^{200}(r)$ values (up to 1.5×10^{10} J m^{-2}). High $HCA_{1200}^{200}(r)$ values (larger than 5×10^9 J m^{-2}) can be traced along the northern route up to the area near 20°W. The southern route is characterized, in general, by significantly lower $HCA_{1200}^{200}(r)$ (in average, a factor of 2–3 lower). From Figure 6a it appears that the major route for ARs heat transport in the South Atlantic Ocean is the northern route. No clear pattern emerges in the western South Atlantic Ocean where ARs from both route show values between 2 and 5×10^9 J m^{-2}.

The fact that the layers below the seasonal thermocline are stable during the whole year leads us to consider only the subsurface fraction (below 200 m) of $HCA(r)$. However, we need to assess the percentage of the neglected $HCA(r)$ in doing so. With this in mind, we compute the percentage of the $HCA_{1800}^{0}(r)$ contribution stored in the upper 200 m, defining $z_{up} = 0$ m and $z_{low} = 200$ m in Equation 2. It should be noted, however, that 30 of the 221 Argo profiles in ARs do not reach depths greater than 1,800 m and therefore the contribution cannot be calculated for them.

$$ContribHCA(r)_{z_{low}}^{z_{up}} = \frac{HCA(r)_{z_{low}}^{z_{up}} \times 100}{HCA(r)_{1800}^{0}}. \quad (2)$$

$ContribHCA(r)_{200}^{0}$ are presented in Figure 6b. The highest upper 200-m $HCA(r)$ contributions are found in the surface-intensified ARs close to the Agulhas retroflection area, along the southern route and close to the American margin. At contrary, the northern route is associated to negative contributions highlighting that these eddies are, in average, deeper than the layer of negative temperature anomalies (i.e., positive σ_0 as discussed in the previous section). For 37% (83%) of the profiles, the absolute contribution of the upper 200 m is lower than 10% (20%) of $HCA_{1800}^{0}(r)$. Consequently, in most cases by not including the upper 200-m layer in the $HCA(r)$ estimate, we neglect less than 20% of the HC total value.

Another strong assumption we make is to have fixed a depth of 1,200 m as the lower limit of the HC vertical integration. In doing so, we neglect the fraction of $HCA(r)$ below this depth in contradiction with estimates of ARs vertical extensions reaching greater depths near their area of formation, which is at least 1,600 m (e.g., Arhan et al., 2011; Schmid et al., 2003). To account for the error introduced by neglecting this deep contribution to $HCA(r)$, we compute the fraction of $HCA(r)$ for the depth range 1,200–1,800 m ($ContribHCA(r)_{1800}^{1200}$), defining $z_{up} = 1{,}200$ m and $z_{low} = 1{,}800$ m in Equation 2. In contrast with the distribution for $HCA(r)$ in the upper 200 m, the deep $HCA(r)$ contribution does not display a clear spatial pattern as illustrated in Figure 6c. The results show unambiguously that the deepest layer affects the total value of $HCA(r)$ less than

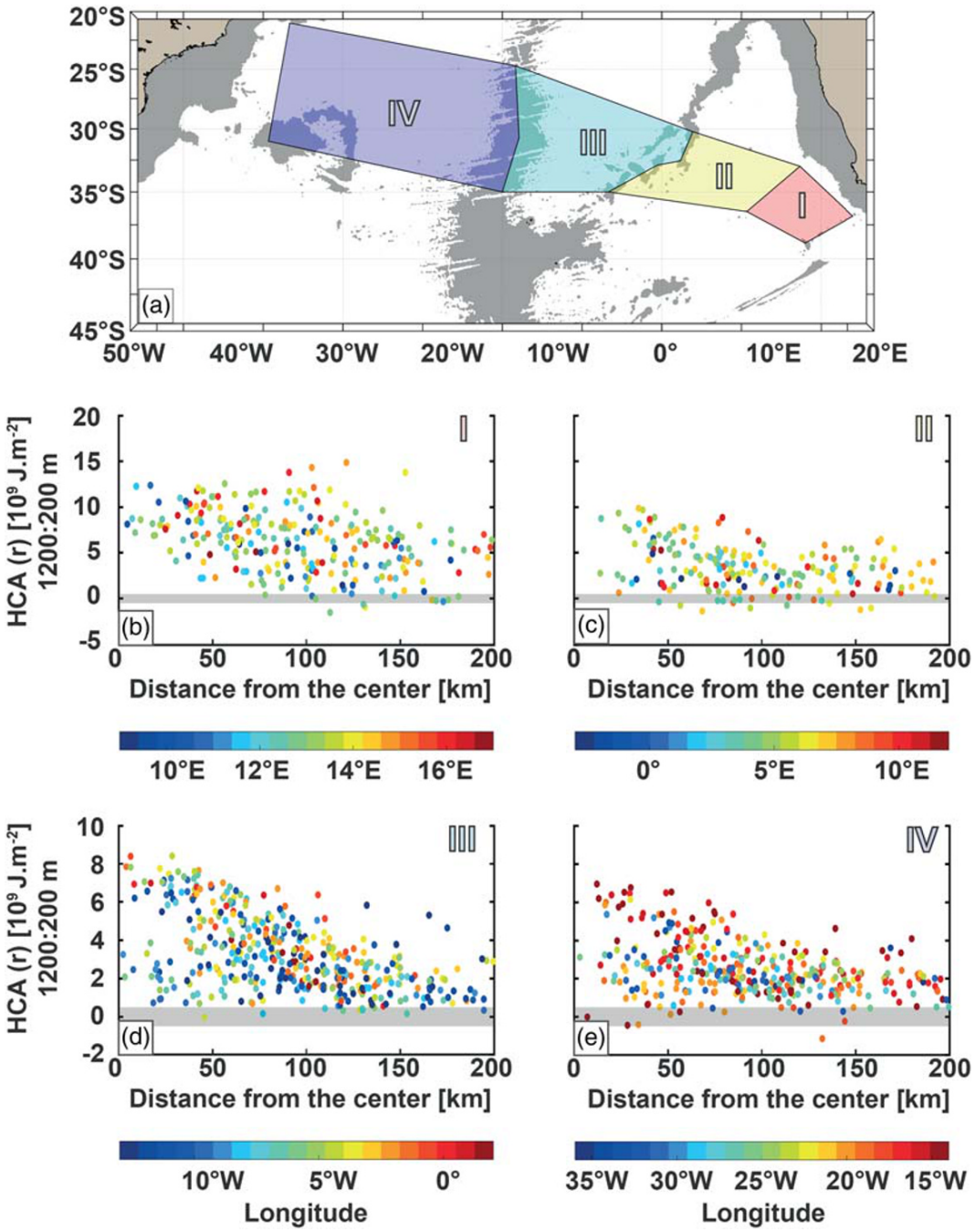

Figure 7. (b–d) $HCA(r)_{1200}^{200}$ computed for all the Argo profiles sampling inside an Agulhas ring (AR) estimated in the four boxes presented in panel (a). The gray shading in panel (a) represents water depths of less than 3,500 m in the ETOPO1 data set (Amante & Eakins, 2009). The gray patches centered around 0 in (b) and (c) indicate the uncertainties of 0.5×10^9 J m^{-2} estimated for $HCA(r)_{1200}^{200}$. The color of each circle in panels (d) and (e) corresponds to the longitude of the sampling.

the upper 200-m layer does. $HCA(r)_{1800}^{1200}$ contributes less than 10% (20%) of the $HCA(r)_{1800}^{0}$ in 81% (99%) of ARs.

We showed by the studying vertical distribution of $HCA_{1800}^{0}(r)$ that $HCA_{1200}^{200}(r)$ accounts for the major proportion of it. Indeed, it accounts for more than 75% of $HCA_{1800}^{0}(r)$ in 75% of the profiles within ARs. To

determine if Agulhas rings $HCA(r)$ is distinct from other eddies, we compare it with that of other anticyclonic eddies detected in the region covered by the study. The middle panel in Figure S1 in the supporting information shows the $HCA_{1200}^{200}(r)$ for the latter that have significant negative σ_0. In the area where most of the ARs are sampled, the $HCA_{1200}^{200}(r)$ for other anticyclones tends to be lower than for ARs. To obtain a broader quantitative view of the whole domain, we compute for each of the 221 selected ARs Argo profiles, the mean and standard deviation (STD) of $HCA_{1200}^{200}(r)$ in the other anticyclonic eddies lying within a distance of 4° in longitude and latitude. The values obtained show that 80% (51%) of ARs have higher $HCA_{1200}^{200}(r)$ than the mean (mean + 1 STD) of surrounding non-AR anticyclones (we refer any interested reader to the lower panel of Figure S1 in the supporting information for a geographical distribution of this comparison)

3.3. HCAs Clustered in Boxes

By selecting ARs, we are choosing eddies whose structure and properties should be closely related. This is in line with the results obtained in the previous sections: ARs show a distinct geographical pattern of surface and subsurface eddies as well as in terms of HCA distribution. This motivates for a clustering of ARs in four geographical boxes (shown in Figure 7a and numbered from I to IV).

The four boxes delineate regions where the HC in the environment is relatively homogeneous (Figure S2a in the supporting information). They are positioned along the ARs route into the Atlantic Ocean and are subdivided according to the main topographic features (the Agulhas, Walvis, and Mid-Atlantic Ridges) as they are expected to influence their eddy structure and properties (e.g., by inducing diapycnal mixing), as discussed by various authors (e.g., Beismann et al., 1999; Nencioli et al., 2018). We have divided the Cape Basin into two separate boxes (I and II in Figure 7a): one representing the southeastern sector where eddy activity is very intense (the so-called Cape Cauldron Boebel et al., 2003) and where $HCA_{1200}^{200}(r)$ has particularly high values and the other corresponding to the northwestern sector of the Cape Basin, which is farther away from the Agulhas Ridge and the Agulhas Current retroflection. Here, ARs are older and have already traveled across the Cape Cauldron area. The two Cape Basin boxes are relatively small compared to the size of the basin as a whole and also in relation to the other two South Atlantic boxes (III and IV in Figure 7a). This is because the Cape Basin exhibits the largest variations in environmental properties, as shown in supporting information Figure S2.

Figures 7b–7e present the value of $HCA_{1200}^{200}(r)$ computed for every Argo profile falling within an AR for each box. The results are plotted as a function of the distance of the profile from the eddy center. Here, we make the assumption that eddies are axisymmetric. Figure 7 shows clearly that in the Cape Basin, the $HCA_{1200}^{200}(r)$ of the ARs (panels b and c) are larger than in the Atlantic basin (panels d and e). However, the dispersion of $HCA_{1200}^{200}(r)$ values is large in all panels. This suggests that $HCA_{1200}^{200}(r)$ is highly variable within the different geographical areas and there is no clear correlation with the distance from the center. Although these boxes are rather larger, no clear regional dependency is evident as shown by the color of the circles representing the longitude for each profile. Figures where circles are colored according to latitude (Figure S3) yield similar results. One exception is Box I where, in the Cape Cauldron area, the latitude seems to have an impact as indicated by the large variations in HC in this box (Figure S2). These results suggest that, even when selecting eddies with similar origin, eddy anomalies are still highly variable.

3.4. Integration of the AR HCA

The large variability in ARs anomalies has to be kept in mind when obtaining the total HCA associated with each eddy as the values of $HCA_{1200}^{200}(r)$ need to be integrated across the entire surface of the eddy, following Equation 3:

$$HCA_{r=0}^{r_{integ}} = 2\pi \int_{r=0}^{r_{integ}} HCA_{1200}^{200}(r) r dr. \quad (3)$$

Because Argo profiles do not sample the entire eddy structure, we need to extrapolate either the values of $HCA_{1200}^{200}(r)$ across its entire width, or, alternatively, the hydrographic properties for the whole eddy volume. The most widely used approach is to define several geographical boxes in which composite eddies are computed (e.g., Chaigneau et al., 2011; Schütte et al., 2016; Yang et al., 2013) such as the boxes presented in Figure 7. This method relies heavily on the assumption that eddy properties and structure are

homogeneous in a specific region, which does not seem to be the case here. This hypothesis has profound impacts on estimates of eddy integrated variables such as the total eddy HCA.

Indeed, considering n eddies, we might expect that $\frac{1}{n}\sum_{i=1}^{n}\left(\int_{r=0}^{r_{integ}} HCA_i(r)rdr\right) \neq \int_{r=0}^{r_{integ}}\frac{1}{n}\sum_{i=1}^{n}(HCA_i(r))rdr$. This is particularly important if eddies of different size are integrated in the composite estimate. This can be demonstrated by considering, as an example, two different eddies: one with a radius larger than 200 km associated with a $HCA(r) = 1$ everywhere and another smaller eddy with a 150-km radius, also characterized by $HCA(r) = 1$. In the case of the second eddy, observations farther than 150 km from its center are not considered as they do not characterize the eddy properties but rather the environment. As a consequence, in the composite derived from these two eddies, $\frac{1}{2}\sum_{i=1}^{2} HCA_i(r)$ would be equal to 1 instead of 0.5 for $r > 150$ km. In this example, the integration in terms of eddy-composite results in an overestimation of HCA of about 30% for $r_{integ} = 200$ km when compared to the estimate obtained by taking the average values of HCA integrated separately for each eddy.

3.4.1. The Reconstruction of the HCA for Individual ARs

One approach to take into account the eddy diversity in estimating HCA_{1200}^{200} is therefore to reconstruct them individually. However, this can be achieved only if the eddies are sufficiently sampled along their trajectory. This type of approach has been already implemented to reconstruct one or more AR hydrographic structures (e.g., Laxenaire et al., 2019; Nencioli et al., 2018; Souza et al., 2011).

In the current study we apply this approach to estimate the HCA_{1200}^{200} of several ARs for each box. This assessment should allow us to better characterize the geographical distribution of HCA_{1200}^{200}. Yet to achieve such a reconstruction, we need to make some assumptions on the eddy shape in order to extrapolate sparse profiles into a full structure. For example, it is very common to assume that ARs have an axisymmetric configuration without any vertical tilt. This assumption has been validated by observations (Van Aken et al., 2003) and numerical simulations (Bettencourt et al., 2012).

A second assumption is to describe the horizontal variations of the hydrographic properties of ARs in terms of a generic function that does not depend on depth. This assumption has been verified, at least at the first order, from observations of eddies in the global ocean by Zhang et al. (2013) and for some ARs by Nencioli et al. (2018). Because to our knowledge, the horizontal dependence between $HCA(r)$ and a fixed horizontal function has not yet been tested, in the following we attempt to validate our approach. For this purpose, for every Argo profile within an AR, we compute the correlation between $HCA_{1200}^{200}(r)$ and the local dynamic-height anomaly (DHA), a proxy of sea surface height anomalies (SSHAs), computed for the same depth interval. The DHA is estimated using the "*geo_trf_dyn_height*" MATLAB function from the GSW Oceanographic Toolbox of the Thermodynamic Equation of SeaWater TEOS-10 (McDougall & Barker, 2011). The results show a strong linear correlation between these two variables with a coefficient of determination (R^2) equal to 0.95. This correlation, which is very likely related to the impact of the thermal expansion of water on DHA, gives us confidence in using a generic function to describe the horizontal shape of the eddies as it was done, for example, by Chelton et al. (2011) on sea level anomalies (SLAs). In this study, we take the Gaussian analytic function given in Equation 4 for ARs $HCA(r)$. The main parameters are $HCA_{1200}^{200}(r = 0)$ and R_0, which controls the width of the Gaussian bell. When applied on ADT maps and by assuming the geostrophic approximation, one can easily show that R_0 in Equation 4 is equal to the R_{Vmax} obtained from the same maps. This type of horizontal function has been used in previous studies to characterize eddy hydrographic properties (e.g., temperature, salinity, and density anomalies) (e.g., Laxenaire et al., 2019), SLA (e.g., Chelton et al., 2011), and pressure anomaly (e.g., Nencioli et al., 2018; Zhang et al., 2013).

$$HCA_{1200}^{200}(r) = HCA_{1200}^{200}(r = 0)e^{-\frac{1}{2}\left(\frac{r}{R_0}\right)^2}. \quad (4)$$

Such a function can only be applied if anomalies are computed using a local climatological profile as HCA needs to go to 0 far from the center. This allows us to use fixed values both for vertical and horizontal integrations avoiding the reconstruction of the eddy over its entire volume. This way, water masses not

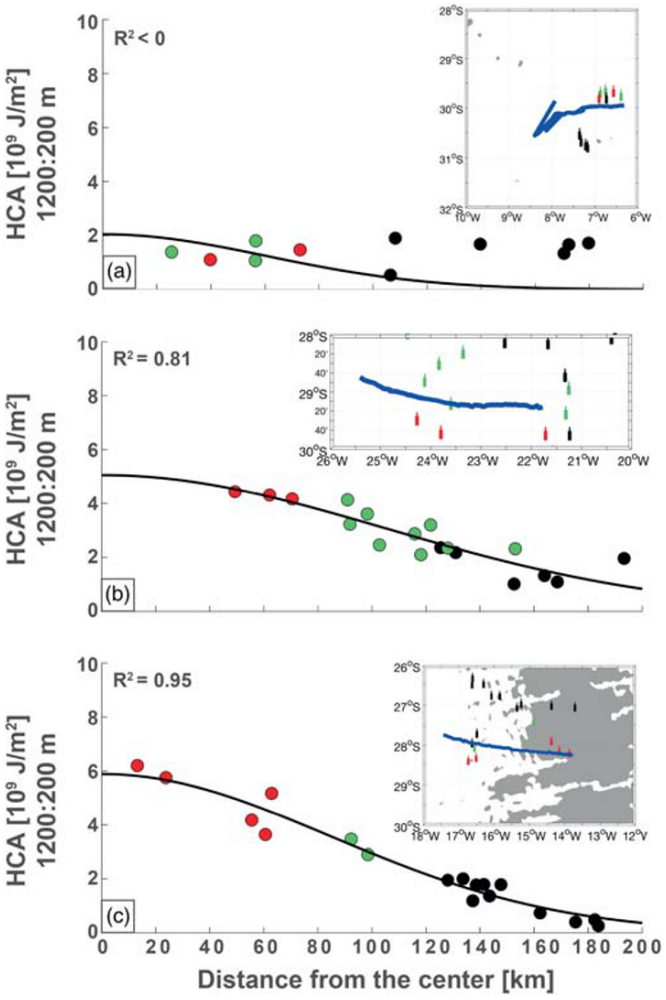

Figure 8. Three examples (panels a–c) of reconstructed $HCA_{1200}^{200}(r)$ and their associated coefficient of determination (R^2) for eddies lying in the Atlantic Ocean. $HCA_{1200}^{200}(r)$ values derived directly from observations are presented as gray circles, while the $HCA_{1200}^{200}(r)$ values achieved using a Lagrangian reconstruction are shown as black lines. The trajectories (in blue) and the position of the associated Argo profiles are presented in a map at the top right corner of each panel. The Argo profiles are drawn in red if they sample the Agulhas rings within their R_{Vmax} contours; in blue if in the eddy but in the R_{Vmax} contour and in black the profiles surfacing in the background within 200 km of the eddy center.

associated with the eddy will not be included properties. This is particularly important as eddies have not a cylindrical shape, and the volume of water trapping is expected to be shallower than 1,200 m far from the center as shown by Laxenaire et al. (2019). To ensure that, Argo profiles surfacing inside neither a cyclone nor an anticyclone that is within 200 km of the center of an AR are included in the reconstructions. This is similar to the approach of Nencioli et al. (2018) and Souza et al. (2011) except that they used 270 km. We set this limit at 200 km as observed ARs are characterized by radii considerably smaller than this value (e.g., Arhan et al., 1999; Casanova-Masjoan et al., 2017; Garzoli et al., 1999; Lutjeharms, 2006). This prevents selecting profiles outside the targeted eddy. In addition, as shown by Amores et al. (2017), eddies tend to be surrounded by eddies of opposite polarity that are not a part of their dynamical structure. To reduce their effect, the Argo profiles within the 200 km where $HCA_{1200}^{200}(r) \leq -0.5 \times 10^9\,\mathrm{J\,m^{-2}}$ (i.e., significantly negative compared to the uncertainty we estimated) are not considered.

It is then possible to fit this function for each segment of AR trajectories sampled by at least two Argo profiles to reconstruct the full $HCA_{1200}^{200}(r)$ for every eddy. However, to prevent large errors in the extrapolation, we prescribe that the horizontal reconstruction of $HCA_{1200}^{200}(r)$ along a segment of ARs trajectories is estimated only if certain criteria are verified:

- The eddy has to be sampled by more than six Argo profiles and, of these, at least three are located in the characteristic core to ensure a good sampling of the eddy interior.
- At least one of the profiles lies within each of the following distance from the center intervals: (center, 50 km), (50 km, 100 km), and (100 km, 200 km) to ensure a good sampling of the different areas of the eddy.
- The Argo profiles should be separated in time by less than 30 consecutive days (i.e., three Argo cycles) to avoid long period of time between vertical samplings.
- The maximum difference in eddy weekly averaged R_{Vmax} (ΔR_{Vmax}) should not exceed 40 km to ensure the eddy did not evolve excessively.
- The period of sampling used for a reconstruction cannot exceed three months to avoid long periods of time during which the eddy properties might evolve.
- The eddy under consideration should not cross any of the limits of the four geographical boxes presented in Figure 7a to ensure a coherence with the HCA pattern identification described in the previous sections.

We compute the horizontal function for $HCA(r)$ by minimizing the fitting of Equation 4 to the observations. We make use of the trust-region reflective algorithm (Branch et al., 1999) with the function lsqcurvefit of the MATLAB library. For each reconstruction, the initial value of R_0 is fixed to the average R_{Vmax} and constrained by $R_{\mathrm{Vmax}} \pm 20$ km, which corresponds to the criterion of the maximum of R_{Vmax} used for the identification of the AR segments that could be reconstructed. A local minimum of the residuals obtained from the least squares method is often derived when fitting this function. To prevent this, five different fittings are tested where the initial value of $HCA_{1200}^{200}(r=0)$ increases by 2×10^9 from 2×10^9 to $20 \times 10^9\,\mathrm{J\,m^{-2}}$. The coefficient providing the lowest squared 2-norm of the residual is retained.

Using this method, we are able to identify 69 segments of AR trajectories. While the fitting process aims to overcome errors linked to measurement uncertainties and poor estimation of the distance of the Argo profile from the center, the reconstructed segments might provide unsatisfactory results. This because of various reasons such as the occurrence of eddy splitting and eddy merging. Because of this, the $HCA_{1200}^{200}(r)$ resulting

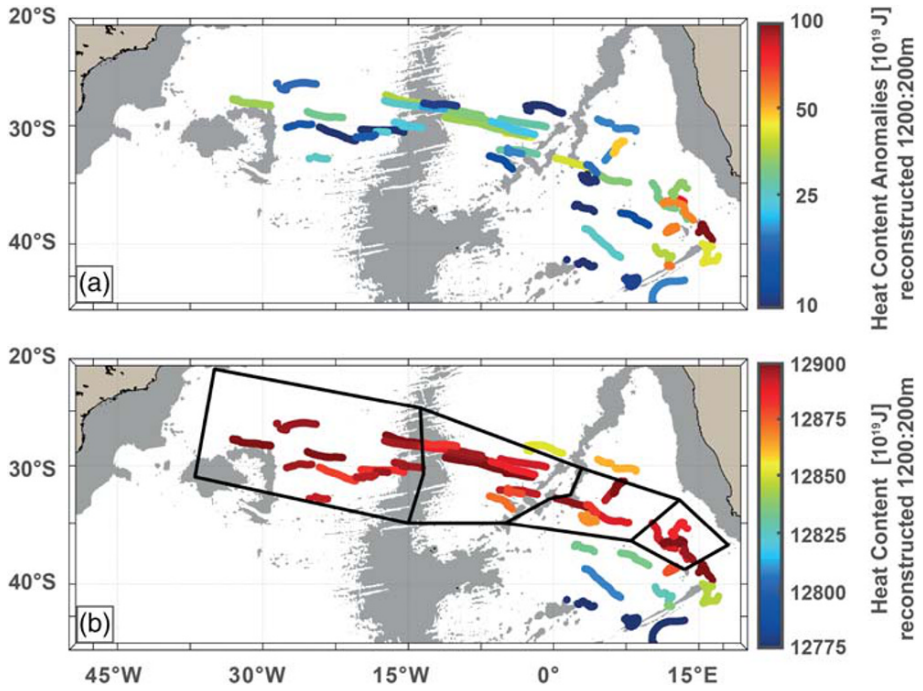

Figure 9. Heat content anomalies (panel a) and heat content (panel b) in the individual reconstructions of Agulhas rings (ARs). The values are repeated at the position of the center derived from the altimetry. The four boxes used to study regionally the AR corridor are also added to the panel (b). The gray shading in each panel represents water depths of less than 3,500 m in the ETOPO1 data set (Amante & Eakins, 2009).

from various profiles might not be completely coherent. To prevent this, following Nencioli et al. (2018), we use the coefficient of determination (R^2) to validate the reconstruction. This coefficient is applied to a non-linear fitting, which prevents it from being used to validate a null hypothesis whereas allowing to qualitatively evaluate the robustness of the fit. Figure 8 shows three examples of $HCA(r)$ reconstruction for ARs segments sampled in the Atlantic Ocean with a similar number of Argo profiles (between 11 and 18).

Figure 8a presents the poorest reconstruction of the three cases associated with a negative R^2. The $HCA^{200}_{1200}(r)$ variations are relatively low, which explains why a flat curve would fit better than the reconstruction resulting in a very low R^2. Figure 8b shows a better reconstruction, yet one point appears to be too far away from the eddy center. The impact of this point, which might sample a nearby structure and therefore not represent the core of the eddy under study, is important on the outer value. If $HCA^{200}_{1200}(r)$ is integrated over the surface of the eddy, the values lying in the outer rim of the eddy affect the result. Hence, attention should be paid to those peripheral points that might lead to large errors in the estimates. Figure 8c shows an example of a particularly adequate reconstruction for $HCA^{200}_{1200}(r)$ as the Argo profiles sample the ARs over a wide range of its radius.

Among the 69 segments for which we implemented the individual reconstruction of $HCA^{200}_{1200}(r)$, 69% are associated with a $R^2 > 0.7$ and 29% with a $R^2 > 0.9$. After a careful examination of the $HCA^{200}_{1200}(r)$ reconstruction for each of the 69 segments, the limit of $R^2 > 0.7$ seems sufficient to grant an adequate functional fitting with the observations. This threshold allows us to select 48 of the 69 initial segments. This criterion is similar to the $R^2 = 0.7$ used by Nencioli et al. (2018) except that those authors used this criterion only for segments for which the minimum distance from the center is larger 50 km, while it is not possible using our method. Indeed, among the 48 segments, there are 23 (10) segments for which the smallest distance of the Argo profiles from the center is less than 25 km (in the range of 40 to 50 km). The median number of Argo profiles used to reconstruct the $HCA^{200}_{1200}(r)$ for the selected AR segments is 10, whereas the maximum number of profiles is 25.

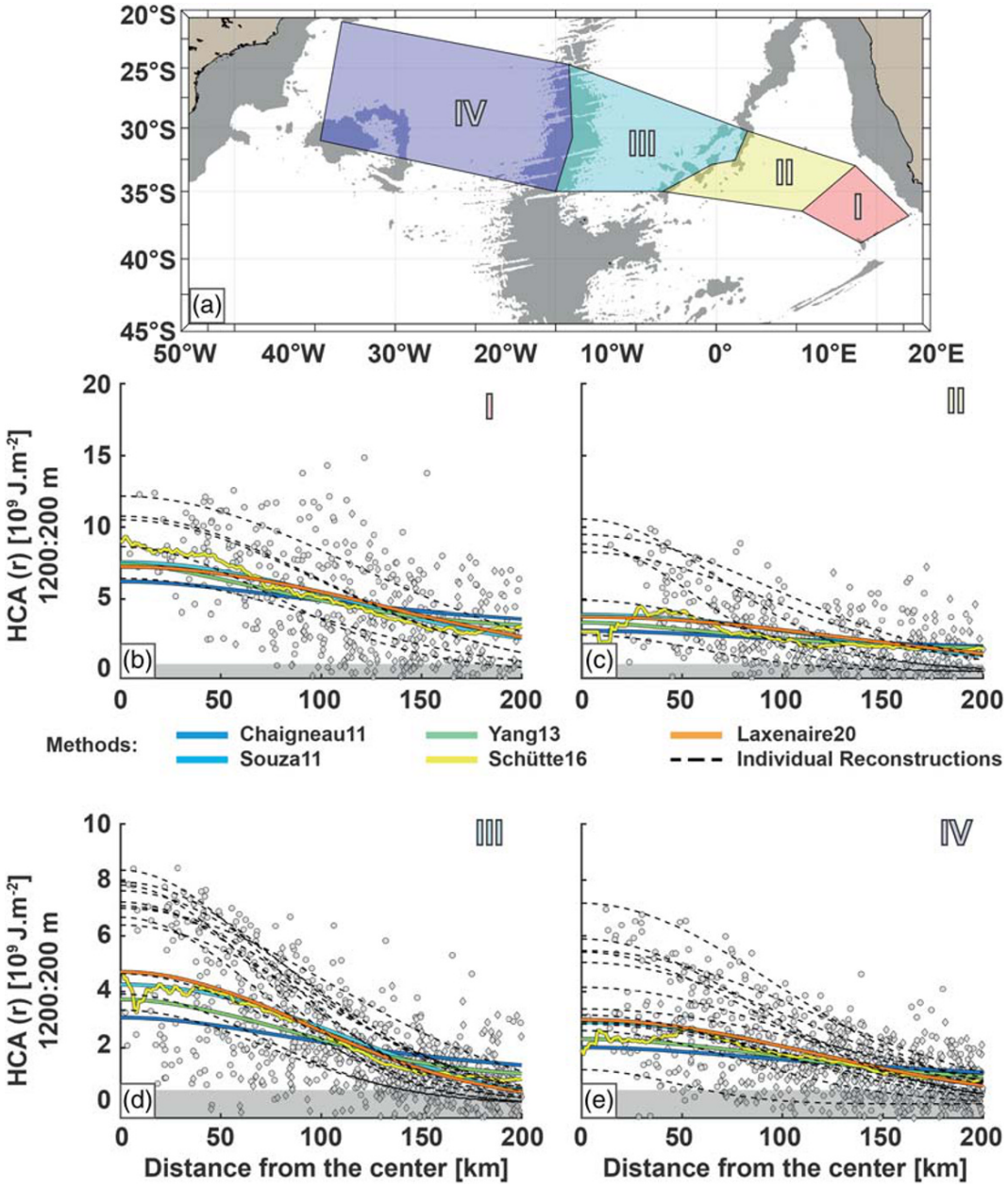

Figure 10. Reconstruction of HCA_{1200}^{200} using the whole set of Argo profiles sampling inside an Agulhas ring (AR; panels b–e) in the four geographical boxes presented in a). The dot indicates $HCA_{1200}^{200}(r)$ profiles in the ARs and diamonds those neither surfacing inside a cyclone or an anticyclone within 200 km of the center of an AR. Each colored thick line in (b) and (c) is associated with a different eddy-composite method of reconstruction, whereas the dashed black lines represent the individual reconstructions. The gray shading in panel (a) represents water depths of less than 3,500 m in the ETOPO1 data set (Amante & Eakins, 2009). The gray patches centered around 0 in (b) and (c) indicate the uncertainties of 0.5×10^9 J m^{-2} estimated for $HCA_{1200}^{200}(r)$.

The eddy-integrated HCA_{1200}^{200} and the total HC_{1200}^{200} obtained by adding the mean $HC_{1200}^{200}(r)$ of reference to $HCA_{1200}^{200}(r)$ for the 48 selected segments are shown in Figure 9. These segments correspond to 33 AR trajectories up to order 4 as shown in Figure S4. For some of these trajectories, more than one AR HC reconstruction can be computed at different stages of the ARs lifetime. This multiple reconstructions cannot be used to study the corresponding AR evolution in time as it is not possible to use local anomalies to do this. Indeed, when comparing the mean $HCA_{1200}^{200}(r)$ variations in Figure 9a and with the mean HC_{1200}^{200} in Figure 9b, it

Table 1
Eddy Integrated HCA_{1200}^{200} Obtained by Applying Different Approaches (Eddy-Composite and Individual Reconstructions) in Each of the Four Geographical Boxes Presented in Figure 10a

		Box I	Box II	Box III	Box IV
Eddy composites	Mean	54×10^{19} J	27×10^{19} J	23×10^{19} J	18×10^{19} J
	STD	1.5×10^{19} J	1.3×10^{19} J	0.6×10^{19} J	0.8×10^{19} J
	$[-\Delta,+\Delta]$	$[17,92]\times10^{19}$ J	$[5,49]\times10^{19}$ J	$[7,41]\times10^{19}$ J	$[5,32]\times10^{19}$ J
Individual reconstructions	Mean	51×10^{19} J	27×10^{19} J	26×10^{19} J	21×10^{19} J
	STD	20×10^{19} J	16×10^{19} J	9×10^{19} J	10×10^{19} J
	Number	5	6	12	12

Note. For each composite, upper and lower bounds of estimation in the 68% confidence interval are provided by, respectively, $+\Delta$ and $-\Delta$.

appears clearly that an important fraction of the HC variations are directly linked to variations in the HC of reference.

Nonetheless, it is possible to identify the reconstructed segments in the Boxes I–IV (Figure 9b) to obtain an estimation of the geographical distribution of the average HCA_{1200}^{200}. Because some of the reconstructed segments do not intercept any boxes, we only use 35 of 48 reconstructed segments. We obtain a mean HCA_{1200}^{200} (STD) of 5.1×10^{20} J (2.0×10^{20} J), 2.7×10^{20} J (1.6×10^{20} J), 2.6×10^{20} J (0.9×10^{20} J), and 2.1×10^{20} J (1.0×10^{20} J), from 5 6, 12, and 12 reconstructions in Boxes I, II, III, and IV, respectively.

3.4.2. The Composite Reconstruction of the HCA and Comparisons of the Two Approaches

To compare the results obtained from the individual reconstructions to the traditional composite methods, we integrate the $HCA_{1200}^{200}(r)$ into composite eddies in each box computed over a fixed grid of 1 km in the radial distance using $HCA_{1200}^{200}(r)$ selected for individual reconstructions (i.e., in ARs and within 200 km of their center). Five composites are obtained for each box by fitting either Equation 4 (hereafter Laxenaire20) or by following four other methods described in Chaigneau et al. (2011) (hereafter Chaigneau11), Yang et al. (2013) (hereafter Yang13), Souza et al. (2011) (hereafter Souza11), and Schütte et al. (2016) (hereafter Schtte16). We refer each interested reader to the supporting information where they are briefly described.

Figure 10 presents the different estimates for $HCA_{1200}^{200}(r)$ computed according to the various techniques in each of the four boxes. Although there are differences between the $HCA_{1200}^{200}(r)$ in the composites, their overall appearance is rather similar. In comparison, the estimates obtained using the individual reconstruction method are significantly different from any of the eddy-composite methods. In general, the individual reconstructions provide $HCA_{1200}^{200}(r=0)$ that are higher than the eddy-composite approaches, whereas they are smaller at the outer rim of eddies. The individual reconstructions seem to better capture the $HCA_{1200}^{200}(r)$ properties in the boxes. However, the number of individual reconstruction, and therefore their representativeness in terms of eddy varieties, is not homogeneous for all boxes. They are relatively well distributed capturing the variations of $HCA_{1200}^{200}(r)$ within Boxes III and IV where 12 AR segments were reconstructed. However, only 5 and 6 reconstructions were possible in each of the other two boxes (i.e., I and II).

To obtain a more quantitative comparison between the different approaches, we integrate HCA_{1200}^{200} values across the first 200 km for each eddy following Equation 3. The averaged HCA_{1200}^{200} obtained for the eddy composites and in the individual reconstructions are presented in Table 1 (details of HCA_{1200}^{200} composite estimates and associated uncertainties are provided in Table S1). Eddy composites estimates result once again very similar (the associated STD is less than 5% of the HCA_{1200}^{200} mean value in each box). For each composite, an estimation of the 68% confidence interval (CI) at a fixed grid of 1 km along the radial distance is computed and the integration is realized by taking $HCA_{1200}^{200}(r)\pm$ CI. This gives a crude estimation of the confidence in the HCA_{1200}^{200} integration. The upper ($+\Delta$) and lower ($-\Delta$) bounds of each method are averaged and provided in the Table 1. As expected from $HCA_{1200}^{200}(r)$ variability (Figure 10), the CI results in large variations of HCA_{1200}^{200} somewhere in between 5 times smaller and 2 times larger of the mean in each box.

The HCA_{1200}^{200} mean value obtained by applying the individual reconstruction approach is close to that obtained via the eddy-composite approaches. However, the STD obtained for the former vary between 20% and 60% of the mean HCA_{1200}^{200} in each box. This indicates large variations in hydrographic properties

Table 2
Eddy Integrated $HC^{200}_{1200}(r=0)$ Computed From the $HCA^{200}_{1200}(r=0)$ for the Reconstructed Agulhas Rings and the Environment Local Average HC

		Box I	Box II	Box III	Box IV
Eddy composites	Mean	30×10^9 J m^{-2}	27×10^9 J m^{-2}	28×10^9 J m^{-2}	27×10^9 J m^{-2}
	STD	1×10^9 J m^{-2}	0.8×10^9 J m^{-2}	0.7×10^9 J m^{-2}	0.5×10^9 J m^{-2}
	$[-\Delta,+\Delta]$	[27,33] $\times10^9$ J m^{-2}	[25,28] $\times10^9$ J m^{-2}	[26,29] $\times10^9$ J m^{-2}	[26,28] $\times10^9$ J m^{-2}
Individual reconstructions	Mean	32×10^9 J m^{-2}	31×10^9 J m^{-2}	30×10^9 J m^{-2}	29×10^9 J m^{-2}
	STD	2×10^9 J m^{-2}	3×10^9 J m^{-2}	2×10^9 J m^{-2}	2×10^9 J m^{-2}
	Number	5	6	12	12
Climatology	Mean	22×10^9 J m^{-2}	23×10^9 J m^{-2}	24×10^9 J m^{-2}	25×10^9 J m^{-2}
	STD	0.8×10^9 J m^{-2}	0.6×10^9 J m^{-2}	0.4×10^9 J m^{-2}	0.4×10^9 J m^{-2}

Note. $HCA^{200}_{1200}(r=0)$ is obtained by applying different approaches (eddy composite and individual reconstructions) in each of the four geographical boxes presented in Figure 10a. The averaged HC computed from the local climatological profiles is indicated in the last row. For a better readability, we subtracted 1×10^{12} J m^{-2} to each values.

between different ARs as it is also suggested by the CI in the composites. Nonetheless, all the methods show that the ARs HCA^{200}_{1200} associated to the AR decreases along their route.

These results are however sensitive to the HC estimate for the environment that evolves geographically (Figure S2). Therefore, while being meaningful to study the local impact of ARs in the different regions, it is not possible to directly compare HCA^{200}_{1200} estimates for the different box areas. We also cannot truthfully compare the total HC^{200}_{1200} values, as the eddies are not expected to be barotropic and cylindrical in structure. Hence, especially far from the eddy centers, we expect only a small fraction of the water column to be impacted by the eddy presence. This is not a constraint for HCA^{200}_{1200} estimates themselves because anomalies should fall to 0 outside the eddy's area of influence, but it prevents any simple integration with the local average value of the environment HC^{200}_{1200} and therefore any robust comparison among remote eddies.

Close to the eddy center, ARs are expected to extend at least to 1,200 m within the Cape Basin (e.g., Duncombe Rae et al., 1996; McDonagh et al., 1999) and in the South Atlantic Ocean (e.g., Laxenaire et al., 2019; Nencioli et al., 2018; Souza et al., 2011). Therefore, a qualitative comparison among ARs in different regions can be undertaken comparing the value of the HC at their center (i.e., $HC^{200}_{1200}(r=0)$). The resulting $HC^{200}_{1200}(r=0)$ values for the eddies and those corresponding to the local climatological profiles are presented in Table 2. The overall trend of $HC^{200}_{1200}(r=0)$ in the climatology is a gradual increases along the AR corridor, whereas a gradual decreases is visible for individual reconstructions and rather constant values in the eddy composites in Boxes II to IV. The results for the individual reconstructions appear to be in line with a better account of the eddy center properties (see Figure 10) as already discussed.

3.5. ARs Heat Transport Across the South Atlantic Ocean

The estimates of HCA^{200}_{1200} can be used to compute the heat transport achieved by ARs. This cannot be robustly undertaken in the Cape Basin because the geographical boxes we define do not cover this basin entirely and $HC(r)$ shows a very large variability. However, it seems legitimate to evaluate such a transport in the center of the South Atlantic Ocean since the boxes cover the entire AR corridor (Figure 1).

The classic heat transport estimates for ARs are achieved by multiplying the observed or reconstructed temperature and the volume of one or two eddies by the average number of eddies spawned at the Agulhas retroflection (e.g., Souza et al., 2011). However, the number of ARs crossing a specific geographical line extending over the Cape Basin and the South Atlantic Ocean per year decreases when moving away from the Agulhas Ridge. For example, according to the trajectories reconstructed with our algorithm, 3.5 ARs enter Box III every year but only 2.6 leave it. Hence, on average, 0.9 ARs per year disappear from the altimetric field in this region. Interpreting this disappearance as the dissipation of ARs in this box and taking the averaged values of HCA^{200}_{1200} obtained using the 11 individual reconstructions ±STD (mean $[-\Delta,+\Delta]$ obtained in eddy composites), the dissipation of ARs results in a transfer of $0.7\pm0.3\times10^{-2}$ PW ([0.2,1.2]$\times10^{-2}$ PW) to the ocean interior. Using the same method, we obtain a transfer of $0.7\pm0.4\times10^{-2}$ PW ([0.2,1.1]$\times10^{-2}$ PW) in Box IV where 1.1 ARs disappear per year.

Another possible estimate of AR heat transport can be achieved by considering the average difference between the number of ARs entering and exiting each box per year. This estimate would correspond to the zonal transport of heat across each box. In average around three ARs cross Box III each year, which accounts for a subsurface heat transport of $2.5 \pm 0.9 \times 10^{-2}$ PW ($[0.7,4.0] \times 10^{-2}$ PW) obtained from the averaged HCA_{1200}^{200} in the individual reconstructions ±STD (mean $[-\Delta,+\Delta]$ obtained in eddy composites). Using the same method, we obtain a subsurface heat transport of $1.4 \pm 0.7 \times 10^{-2}$ PW ($[0.3,2.1] \times 10^{-2}$ PW) by the two ARs per year that cross Box IV.

4. Discussions

In this study, several analyses were carried out to finally estimate the subsurface heat transported by ARs across the South Atlantic and the heat they release into the environment during their journey. Although many efforts have been made to support the results presented here, they are limited by many factors such as the ability to correctly identify trajectories from altimetry maps, uncertainties in the position and measurements of Argo profiles, and the ability of the proposed methods to characterize the hydrographic structures of these eddies. Therefore, the major impact of these limitations should be discussed and the resulting estimates should be put into perspective with other attempts described in the literature.

4.1. Identification of ARs and Characterization of Their Vertical Structure

The first major parameter of this work is the definition adopted to identify the Agulhas rings. This is particularly important because we evaluate the heat transport associated to these eddies in the South Atlantic and thus far from their spawning region, southwest of Africa, where they are initially identified. In particular, many authors (e.g., Guerra et al., 2018; Souza et al., 2011) have identified Agulhas rings as anticyclonic eddies detected near or north of 30°S in the Cape Basin. To avoid the uncertainty linked with identifying Agulhas rings far from the Agulhas retroflection, we define them as those anticyclonic eddies whose trajectory can be backtracked to the retroflection by taking into account splitting events, hence using a Lagrangian approach. Accounting for eddy splitting events, for example, is important in this framework, as at least a fraction of the Indian Ocean water trapped in the initial ring will be transferred to the newly formed eddies. This choice is supported by numerous description of the splitting of Agulhas rings in the literature (Arhan et al., 1999; Baker-Yeboah et al., 2010; Boebel et al., 2003; Byrne et al., 1995; Dencausse et al., 2010a; Schouten et al., 2000). However, in this study, we have not limited the number of splitting, which may lead to a question: "Is it relevant to consider that after many splitting, a significant fraction of the water volume of the eddies still comes from the Indian Ocean?" In the present study, we have reconstructed Agulhas ring trajectories (what we define with the acronym ARs) up to an order 10 in which the order quantitatively indicates the number of splitting events necessary to associate a trajectory to a Agulhas ring in the traditional sense. However, the hydrographic properties of such high-order ARs have a relatively small impact on the resulting estimates since more than 94% of Argo profiles sample ARs of order 2 or less and only 3 of the 48 individually reconstructed eddies have an order 3 or 4 (Figure S4a in the supporting information). Furthermore, the numbers of trajectories passing through the sections of interest (shown in Figure 1) become 6.6, 3.4, 2.5, and 1.2 for, respectively, Boxes A to D if only ARs of order 4 or less are taken into account. Thus, we could limit our analysis to ARs of order 4 or less without changing the scope of the results.

The best justification for our choice is provided by the significantly different hydrographic properties near the center of the selected eddies compared to other anticyclonic eddies in the region. This is particularly true because we are only comparing anticyclonic eddies that have subsurface anomalies larger than the uncertainty defined for the ARs that are deliberately high. Our results show that ARs are, on average, associated with higher subsurface HCAs and that a clear geographical separation between surface- and subsurface-intensified ARs appears (Figure 5), whereas this is not as obvious for other structures (Figure S1a in the supporting information). However, a particularly high density of subsurface-intensified non-AR anticyclonic eddies is visible west of the Walvis Ridge. These might be ARs not identified by our method, in the same way as those firstly detected in the Cape Basin instead of near the Agulhas retroflection by other authors (e.g., Guerra et al., 2018; Souza et al., 2011). In addition, Pegliasco et al. (2015) have shown that anticyclonic eddies formed in the Benguela Upwelling can be either surface or subsurface intensified. They tracked these eddies west to 10°W and north of 30°S, which also makes them serious candidates for the subsurface eddies found in this region.

We believe that this separation between surface- and subsurface-intensified ARs is particularly important. Indeed, Souza et al. (2011) used the surface signature of ARs to describe their vertical mean temperature anomalies. But, as Laxenaire et al. (2019) show by reconstructing the evolution of the hydrographic properties of a particular AR, the surface signature of an AR decreases considerably as it leaves the surface while it is still associated with large subsurface hydrographic anomalies and velocities. Moreover, while most ARs reported along the southern route are classified as unspecified, the northern route is clearly composed of subsurface-intensified ARs as indicated by observations from dedicated oceanographic cruises (Arhan et al., 1999; Garzoli et al., 1999). These results suggest that most ARs subside at some point along their route and that in the South Atlantic they propagate as subsurface eddies. The transition from the surface to the subsurface appears to occur as ARs cross the Walvis Ridge and enter the South Atlantic Ocean (Figure 5a). The regional upper-layer density field in the World Ocean Atlas (Locarnini et al., 2019; Zweng et al., 2019) (Figure S5 in the supporting information) shows that ARs cross outcropping isopycnals as they drift in the South Atlantic. This can act as a surface layer of light water below which the surface-intensified eddies have to move along their course as shown by Herbette et al. (2004) from numerical simulations.

4.2. ARs HC

While Argo floats have drastically improved the sampling of the upper 2,000 m of the world ocean, their spatiotemporal coverage is not yet sufficient to document mesoscale dynamics extensively. For example, any three-dimensional eddy reconstruction is possible only if there are a sufficient number of vertical profiles sampling individual structures (e.g., Nencioli et al., 2018; Souza et al., 2011). In an attempt to overcome this limitation, the vertically integrated HC anomaly was calculated instead of reconstructing the vertical structure of the eddy. This approach is particularly appealing as HC anomalies showed to be highly correlated with dynamic-height anomalies, a proxy of sea SSHAs. This motivates the use of a generic function based on such anomalies to reconstruct the HC in eddies as it has been done the SSHA (Chelton et al., 2011).

We have empirically estimated that a minimum number of six Argo profiles sampling a vortex uniformly and located at different distances from its center is a good compromise between the robustness of HCA estimates and the number of reconstructions obtained. This small number of profiles is not yet sufficient to obtain a precise value for the HCA. Nonetheless, it has made it possible to extract the main ARs HC changes along their path.

For the sake of completeness, different eddy composites, based on methods described in the literature (e.g., Chaigneau et al., 2011; Schütte et al., 2016; Souza et al., 2011; Yang et al., 2013), were computed to contrast the results obtained in estimating the ARs HCA by applying different approaches in four regions covering the routes of these eddies across the Cape Basin and the South Atlantic Ocean. Overall, these estimates give similar results and compare well with those we obtained by achieving individual eddy HCA reconstructions. The two approaches highlighted the large variations in the properties of ARs in the selected areas. This is true for both the STD of individual reconstructions and for the HCA-averaged values.

While our estimate of ARs HC is not appropriate to study the evolution of the eddy properties as we use local anomalies, it provides a characterization of the evolution of the total HC per square meters in the center of the eddy. Table 2 shows a clear HC decrease in the center of individual eddies along their trajectory in the South Atlantic basin. This is consistent with Nencioli et al. (2018) recent results documenting the decrease in density anomalies at the center of ARs along their path in the South Atlantic Ocean. These changes in ARs may be the results of numerous processes acting during their journey and are most likely the combination of local air-sea, eddy-eddy, and eddy-topography interactions as discussed in the literature (e.g., Arhan et al., 1999, 2011; Nencioli et al., 2018; Schütte et al., 2016; Yang et al., 2013).

4.3. ARs Heat Transport

In this study, we compute the subsurface heat transport induced by the advection of transformed warms Indian Ocean water by ARs. $2.5 \pm 0.9 \times 10^{-2}$ PW ($[0.7,4.0] \times 10^{-2}$ PW) and $1.4 \pm 0.7 \times 10^{-2}$ PW ($[0.3,2.1] \times 10^{-2}$ PW) across the eastern (Box III) and western (Box IV) South Atlantic areas, respectively. These values are lower than the 7×10^{-2} PW proposed by Souza et al. (2011) and the 3×10^{-2} to 8×10^{-2} PW estimated by Gründlingh (1995). However, comparisons are difficult as Gründlingh (1995) and Souza et al. (2011) estimates were obtained by computing the number of ARs entering the Cape Basin per year, whereas in our

study we only account for those ARs effectively leaving the Cape Basin and entering the South Atlantic Ocean. These eddies have undergone merging and splitting events (e.g., Dencausse et al., 2010a; Laxenaire et al., 2018, 2019), strong air-sea exchanges (e.g., Arhan et al., 2011), and interactions with topography (e.g., Beismann et al., 1999; De Steur & Van Leeuwen, 2009). It is therefore reasonable to suggest that they would account for a lower heat transport than that achieved by retaining the total number of ARs spawned by the Agulhas retroflection. This is indeed supported by the decrease of HC we described at the center of these eddies.

In addition, the transfer of HC from the ARs to the ocean interior in specific region was estimated by taking into account the disappearance of ARs from the altimetric maps. These estimates are $0.7 \pm 0.3 \times 10^{-2}$ PW ($[0.2,1.2] \times 10^{-2}$ PW) and $0.7 \pm 0.4 \times 10^{-2}$ PW ($[0.2,1.1] \times 10^{-2}$ PW) in the eastern (Box III) and western (Box IV) South Atlantic areas, respectively. ARs that cross the entire South Atlantic basin are observed to propagate mostly southward with the South Brazil Current (Byrne et al., 1995; Guerra et al., 2018; Laxenaire et al., 2018). This suggests that most of the ARs spawned by the Agulhas Current do not directly participate to the Meridional Overturning Atlantic Circulation, but instead, they release their heat gradually in the South Atlantic Ocean interior.

One major limit of our study in evaluating the heat transport through and to specific regions is the capacity of altimetric maps to account for the whole spectrum of ARs. That said, when comparing with the results obtained in previous studies and in particular those discussed in the recently published work by Guerra et al. (2018), our estimate accounts for a slightly larger number of ARs crossing the South Atlantic Ocean. Indeed, Guerra et al. (2018) enumerate 2.5 and 1.7 ARs crossing the meridian 10°W and 20°W, respectively, whereas, in the same latitudinal band, our estimates suggest that, on average, 2.6 ARs cross the Mid-Atlantic ridge near 15°W. Still, our estimates are restricted by the signature of such eddies over the altimetry fields independent of the eddy detection methods. Indeed, it was shown by Bashmachnikov and Carton (2012), using both observation and a quasi-gesotrophic framework, that the Meddies, which are well-documented subsurface anticyclonic eddies containing Mediterranean water while drifting in the South Atlantic, have a surface signature controlled by their intensity and their depth. Consequently, we can expect, as stated, for example, by Guerra et al. (2018), that some ARs lose their surface signature while subducting if their intensity is not large enough, and thus, they cannot be followed by our method.

Another possible shortcoming of this work lies in the definition we adopted for the eddy heat transport that we associated with the advection of water masses within the moving eddies identified as coherent structures (known as "eddy drift transport," Hausmann & Czaja, 2012). Recent studies suggest that other processes might impact such a transport. For example, some authors (e.g., Amores et al., 2017; Hausmann & Czaja, 2012; Roemmich & Gilson, 2001; Souza et al., 2011) have highlighted that the nonalignment between the eddy azimuthal speeds and hydrographic anomalies can result in a net meridional transport (defined as the "swirl heat transport" by Hausmann & Czaja, 2012). By comparing these two types of transport via the reconstruction of 16 different ARs, Souza et al. (2011) obtained comparable values for "eddy drift transport" and "swirl heat transport." Recently, the "eddy drift transport" has been revisited and its amplitude slightly reduced (e.g., Wang et al., 2015, 2016). However, it is worth noting that these results are based on algorithms that are strongly dependent on the absolute values of the azimuthal velocities associated with the eddy. In particular, the surface signature of the eddy velocities might not be representative of the eddy-core velocities if the eddy is subsurface-intensified. Besides, ARs show a clear coherent eddy behavior as they advect along their course numerous surface drifting buoys (e.g., Laxenaire et al., 2018; Schmid et al., 2003) and Lagrangian subsurface floats (e.g., Boebel et al., 2003; Laxenaire et al., 2019; Nencioli et al., 2018; Schmid et al., 2003; Souza et al., 2011).

5. Conclusions

In this paper, we have applied an eddy detection and tracking algorithm to identify ARs from daily satellite ADT maps. By colocating the identified eddies with every available in situ Argo float profile, we have investigated their vertical structure and associated HC and transport.

Our results suggest a regional characterization for the vertical structure and properties of ARs. The resulting pattern is an abundance of surface-intensified rings, with a deep ML, in the Cape Basin. They become

subsurface-intensified eddies in the South Atlantic Ocean once they leave the Cape Basin through the Walvis Ridge.

A second aspect that emerges from this work is that the majority of ARs HCAs are stored in the 200- to 1,200-m vertical layer. By calculating the HCAs in this interval and by identifying segments of well-sampled ARs trajectories, we obtained 48 individual reconstructions of HCAs. We also computed ARs HCAs using five different eddy composites approaches in four areas along the AR corridor in the South Atlantic Ocean. The results compare relatively well, but the individual reconstruction method is the only one showing a net decrease in the eddy HCA along the eddies route (i.e., from east to west). Moreover, we computed the total HC at the center of each AR for which the reconstruction was possible. It shows a slow but progressive heat dissipation for these eddies during their journey across the South Atlantic Ocean.

Based on these individual reconstructions (and [lower,upper] bounds of estimated CIs in the eddy composites), we compute a zonal subsurface heat transport associated with these ARs of $2.5 \pm 0.9 \times 10^{-2}$ PW ($[0.7,4.0] \times 10^{-2}$ PW) and $1.4 \pm 0.7 \times 10^{-2}$ PW ($[0.3,2.1] \times 10^{-2}$ PW) across the eastern and western South Atlantic areas, respectively. And, by taking the dissipation of the AR in each box into account, a transfer of heat of $0.7 \pm 0.3 \times 10^{-2}$ PW ($[0.2,1.2] \times 10^{-2}$ PW) to the ocean interior is estimated in the eastern part of the South Atlantic and of $0.7 \pm 0.4 \times 10^{-2}$ PW ($[0.2,1.1] \times 10^{-2}$ PW) in the western part.

While many efforts have been made to carefully identify the properties of eddies and to reconstruct their three-dimensional properties, this study underlines that observations are still limited in their coverage and therefore their capacity to allow complete monitoring of eddies and accurate estimates of the hydrographic properties carried by eddies, as well as their evolution along the way, is also limited. Complementary studies using similar techniques applied to three-dimensional high-resolution ocean simulation fields could be used to corroborate the methods and results presented here and further develop our knowledge and estimates of eddy dynamics and transports.

Appendix A: Estimation of the Hydrographic Uncertainties

By following the Guide to the expression of uncertainty in measurement (GUM) (BIPM, 2008), Dai and Zhang (2018) assessed the main sources of uncertainties converting in situ measurements of the former version of the 0.25° × 0.25° decades-average WOA (1955–2012) using the GSW Oceanographic Toolbox. By detailing the different uncertainty components, they obtained a vertically averaged mean uncertainty in the off-shore part of the Southern Atlantic of about 1.4 db for pressure, about 0.005 g kg^{-1} for S_A (using 0.0017 psu for S_P), about 0.002°C for Θ (using 0.002°C for T) and about 0.005 kg m^{-3} for density (ρ). The uncertainties used by these authors for pressure and T measurements are comparable to those specified for the delayed-mode Argo profiles but not the one for S_P that was lower by nearly 1 order of magnitude (i.e., 0.0017 psu instead of 0.01 psu in Argo). As S_A uncertainty is independent of those on Θ and ρ, it is possible to directly compute the S_A following Dai and Zhang (2018) using the uncertainty for S_P in the Argo profiles resulting into a mean uncertainty of 0.07 g kg^{-1} for S_A. However, Θ and ρ uncertainties are dependent from S_A. This drastically complexifies their determination. As the complete computation of uncertainties is out of the scope of this study, we give an estimate of the resulting uncertainty. For Θ, the uncertainties obtained by Dai and Zhang (2018) are equal to the one for T. However, due to the dependence on S_A that have uncertainties of 1 order of magnitude larger in Delayed Mode Argo, we would like to be conservative by defining a large uncertainty of 0.02°C for Θ (i.e., 10 times the one for T). For density, an estimation can be obtained using the law of propagation of uncertainty (BIPM, 2008) in the linear equation of state for sea water. For example, the uncertainty of 0.005 kg m^{-3} for ρ obtained by Dai and Zhang (2018) is very close to the one of 0.004 kg m^{-3} obtained applying this method to their uncertainties for Θ and S_A. Thus, our estimation of the accuracy computed in the Argo profiles result into uncertainties of about 0.07 g kg^{-1} for S_A, 0.02°C for Θ, and about 0.05 kg m^{-3} for σ_0 that we assume to be similar for ρ.

For the anomaly profiles, the uncertainties on the averaged data given in WOA18 have to be assessed. Due to the averaging process, the relevant uncertainties are not obtained adding independent uncertainty of each measurement but the mean standard error. The standard errors of the mean fields are given at each depth for both T and S_P in WOA18. These errors are averaged in each local climatological profile that results into a mean uncertainties around 0.1°C for T and 0.02 psu for S_P with maximum errors close to the surface and

minimum ones at deepest depth. While the one for the S_P is similar to the one in Argo resulting into an averaged uncertainty of 0.07 g kg^{-1} for S_A, the uncertainty for T is 2 orders of magnitude larger than in Argo profiles. We assume in this case that the uncertainty for Θ is dominated by the large values of the one for T and thus fix it to 0.1°C. By using the linear equation of state, an uncertainty 0.06 kg m^{-3} is estimated for ρ. Finally, using the propagation of uncertainty (BIPM, 2008) combining those for observations and local climatological profiles and rounding numbers to the nearest higher tenth to be restrictive, the uncertainties used in this study for the anomalies of the Argo profiles are 0.1 g kg^{-1} for S_A, 0.1°C for Θ, and 0.1 kg m^{-3} for σ_0.

Data Availability Statement

The database produced for this paper and scripts to reproduce the main figures presented in the results are available at the following website (https://vesg.ipsl.upmc.fr/thredds/catalog/IPSLFS/datapapers/Laxenaire_Database_AR_HCA/catalog.html). The gridded satellite altimetry data we used in this work were produced by SSALTO/DUACS and distributed by the Copernicus Marine Environment Monitoring Service. The Argo data were collected and made freely available by the International Argo Program and the national programs that contribute to it (https://coriolis.eu.org and http://www.argo.ucsd.edu). The Argo Program is part of the Global Ocean Observing System (GOOS). The World Ocean Atlas was created and made freely available by a dedicated research group at the National Oceanographic Data Center thanks to a grant from the NOAA Climate and Global Change Program (https://www.nodc.noaa.gov/OC5/woa18).

Acknowledgments

This work was supported by the European Union Horizon 2020 research and innovation program under Grant Agreement 633211 (AtlantOS), the TOEddies CNES-TOSCA research grant, and the projet SAMOC (11- ANR-56-004) for S. S. and R. L. and the ANR-Astrid Project DYNED-Atlas (ANR-15-ASMA-0003-01) for A. S. and R. L. Many of the Argo floats used in this work have been provided to S.S. by the French national program LEFE GMMC Mercator-Coriolis to be deployed since 2004 in the region within the GoodHope and SAMOC international research projects. We also acknowledge the mesoscale calculation server CICLAD (https://ciclad-web.ipsl.jussieu.fr) dedicated to Institut Pierre Simon Laplace modeling effort for technical and computational support. The authors received several helpful suggestions for improving this manuscript from A. Doglioli and three anonymous reviewers, and their help is gratefully noted.

References

Amante, C., & Eakins, B. (2009). ETOPO1 1 arc-minute global relief model: Procedures, data sources and analysis. NOAA Technical Memorandum NESDIS NGDC-24. National Geophysical Data Center, NOAA https://doi.org/10.7289/V5C8276M

Amores, A., Melnichenko, O., & Maximenko, N. (2017). Coherent mesoscale eddies in the North Atlantic subtropical gyre: 3-D structure and transport with application to the salinity maximum. *Journal of Geophysical Research: Oceans*, *122*, 23–41. https://doi.org/10.1002/2016JC012256

Amores, A., Monserrat, S., Melnichenko, O., & Maximenko, N. (2017). On the shape of sea level anomaly signal on periphery of mesoscale ocean eddies. *Geophysical Research Letters*, *44*, 6926–6932. https://doi.org/10.1002/2017GL073978

Arhan, M., Mercier, H., & Lutjeharms, J. R. E. (1999). The disparate evolution of three Agulhas rings in the South Atlantic Ocean. *Journal of Geophysical Research*, *104*(C9), 20,987–21,005. https://doi.org/10.1029/1998JC900047

Arhan, M., Speich, S., Messager, C., Dencausse, G., Fine, R., & Boye, M. (2011). Anticyclonic and cyclonic eddies of subtropical origin in the subantarctic zone south of Africa. *Journal of Geophysical Research*, *116*, C11004. https://doi.org/10.1029/2011jc007140

Ashkezari, M. D., Hill, C. N., Follett, C. N., Forget, G., & Follows, M. J. (2016). Oceanic eddy detection and lifetime forecast using machine learning methods. *Geophysical Research Letters*, *43*, 12,234–12,241. https://doi.org/10.1002/2016GL071269

Assassi, C., Morel, Y., Vandermeirsch, F., Chaigneau, A., Pegliasco, C., Morrow, R., et al. (2016). An index to distinguish surface-and subsurface-intensified vortices from surface observations. *Journal of Physical Oceanography*, *46*(8), 2529–2552. https://doi.org/10.1175/JPO-D-15-0122.1

BIPM (2008). Evaluation of measurement data: Guide to the expression of uncertainty in measurement.

Baker-Yeboah, S., Byrne, D. A., & Watts, D. R. (2010). Observations of mesoscale eddies in the South Atlantic Cape Basin: Baroclinic and deep barotropic eddy variability. *Journal of Geophysical Research*, *115*, C12069. https://doi.org/10.1029/2010JC006236

Ballegooyen, R. C., Gründlingh, M. L., & Lutjeharms, J. R. (1994). Eddy fluxes of heat and salt from the southwest Indian Ocean into the southeast Atlantic Ocean: A case study. *Journal of Geophysical Research*, *99*(C7), 14,053–14,070. https://doi.org/10.1029/94JC00383

Bang, N. (1970). Dynamic interpretations of a detailed surface temperature chart of the Agulhas Current retroflexion and fragmentation area. *South African Geographical Journal*, *52*(1), 67–76. https://doi.org/10.1080/03736245.1970.10559466

Bashmachnikov, I., & Carton, X. (2012). Surface signature of Mediterranean water eddies in the Northeastern Atlantic: Effect of the upper ocean stratification. *Ocean Science*, *8*(6), 931–943. https://doi.org/10.5194/os-8-931-2012

Beal, L. M., De Ruijter, W. P. M., Biastoch, A., Zahn, R., & SCOR/WCRP/IAPSO Working Group 136 (2011). On the role of the Agulhas system in ocean circulation and climate. *Nature*, *472*(7344), 429–436. https://doi.org/10.1038/nature09983

Beismann, J.-O., Käse, R. H., & Lutjeharms, J. R. (1999). On the influence of submarine ridges on translation and stability of Agulhas rings. *Journal of Geophysical Research*, *104*(C4), 7897–7906. https://doi.org/10.1029/1998JC900127

Bettencourt, J. H., López, C., & Hernández-García, E. (2012). Oceanic three-dimensional Lagrangian coherent structures: A study of a mesoscale eddy in the Benguela upwelling region. *Ocean Modelling*, *51*, 73–83. https://doi.org/10.1016/j.ocemod.2012.04.004

Biastoch, A., Böning, C. W., Schwarzkopf, F. U., & Lutjeharms, J. (2009). Increase in Agulhas leakage due to poleward shift of Southern Hemisphere westerlies. *Nature*, *462*(7272), 495. https://doi.org/10.1038/nature08519

Boebel, O., Lutjeharms, J., Schmid, C., Zenk, W., Rossby, T., & Barron, C. (2003). The Cape Cauldron: A regime of turbulent inter-ocean exchange. *Deep Sea Research Part II: Topical Studies in Oceanography*, *50*(1), 57–86. https://doi.org/10.1016/S0967-0645(02)00379-X

Branch, M. A., Coleman, T. F., & Li, Y. (1999). A subspace, interior, and conjugate gradient method for large-scale bound-constrained minimization problems. *SIAM Journal on Scientific Computing*, *21*(1), 1–23. https://doi.org/10.1137/S1064827595289108

Bryden, H. (1979). Poleward heat flux and conversion of available potential energy in Drake Passage. 1979. 24 P.

Byrne, D. A., Gordon, A. L., & Haxby, W. F. (1995). Agulhas eddies: A synoptic view using Geosat ERM data. *Journal of Physical Oceanography*, *25*(5), 902–917. https://doi.org/10.1175/1520-0485(1995)025<0902:AEASVU>2.0.CO;2

Cabanes, C., Thierry, V., & Lagadec, C. (2016). Improvement of bias detection in Argo float conductivity sensors and its application in the North Atlantic. *Deep Sea Research Part I: Oceanographic Research Papers*, *114*, 128–136. https://doi.org/10.1016/j.dsr.2016.05.007

Carton, X. (2001). Hydrodynamical modeling of oceanic vortices. *Surveys in Geophysics*, *22*(3), 179–263. https://doi.org/10.1023/A:1013779219578

Casanova-Masjoan, M., Pelegrí, J., Sangrà, P., Martínez, A., Grisolía-Santos, D., Pérez-Hernández, M. D., & Hernández-Guerra, A. (2017). Characteristics and evolution of an Agulhas ring. *Journal of Geophysical Research: Oceans*, *122*, 7049–7065. https://doi.org/10.1002/2017JC012969

Chaigneau, A., Gizolme, A., & Grados, C. (2008). Mesoscale eddies off Peru in altimeter records: Identification algorithms and eddy spatio-temporal patterns. *Progress in Oceanography*, *79*(2), 106–119. https://doi.org/10.1016/j.pocean.2008.10.013

Chaigneau, A., Marie, L. T., Gérard, E., Carmen, G., & Oscar, P. (2011). Vertical structure of mesoscale eddies in the eastern South Pacific Ocean: A composite analysis from altimetry and Argo profiling floats. *Journal of Geophysical Research*, *116*, C11025. https://doi.org/10.1029/2011JC007134

Chaigneau, A., & Pizarro, O. (2005). Eddy characteristics in the eastern South Pacific. *Journal of Geophysical Research*, *110*, C06005. https://doi.org/10.1029/2004JC002815

Chelton, D. B., Schlax, M. G., & Samelson, R. M. (2011). Global observations of nonlinear mesoscale eddies. *Progress in Oceanography*, *91*(2), 167–216. https://doi.org/10.1016/j.pocean.2011.01.002

Chelton, D. B., Schlax, M. G., Samelson, R. M., & de Szoeke, R. A. (2007). Global observations of large oceanic eddies. *Geophysical Research Letters*, *34*, L15606. https://doi.org/10.1029/2007GL030812

Cheng, Y., Beal, L. M., Kirtman, B. P., & Putrasahan, D. (2018). Interannual Agulhas leakage variability and its regional climate imprints. *Journal of Climate*, *31*(24), 10,105–10,121. https://doi.org/10.1175/JCLI-D-17-0647.1

Ciani, D. (2016). Subsurface-intensified oceanic vortices: Impact on the sea-surface and mutual interactions (Doctoral dissertation), Université de Bretagne occidentale - Brest. Retrieved from https://tel.archives-ouvertes.fr/tel-01481211

Cui, W., Wang, W., Zhang, J., & Yang, J. (2019). Multicore structures and the splitting and merging of eddies in global oceans from satellite altimeter data. *Ocean Science*, *15*(2), 413–430. https://doi.org/10.5194/os-2018-96

Dai, H., & Zhang, X. (2018). Uncertainties in climatological seawater density calculations. *Journal of Geophysical Research: Oceans*, *123*, 2192–2212. https://doi.org/10.1002/2017JC013427

de Boyer Montégut, C., Madec, G., Fischer, A. S., Lazar, A., & Iudicone, D. (2004). Mixed layer depth over the global ocean: An examination of profile data and a profile-based climatology. *Journal of Geophysical Research*, *109*, C12003. https://doi.org/10.1029/2004JC002378

de Marez, C., P, L., Morvan, M., Carton, X., L'Hégaret, P., Morvan, M., & Carton, X. (2019). On the 3D structure of eddies in the Arabian Sea. *Deep Sea Research Part I: Oceanographic Research Papers*, *150*, 103057. https://doi.org/10.1016/j.dsr.2019.06.003

De Ruijter, W., Biastoch, A., Drijfhout, S., Lutjeharms, J., Matano, R., Pichevin, T., et al. (1999). Indian-Atlantic interocean exchange: Dynamics, estimation and impact. *Journal of Geophysical Research*, *104*(C9), 20,885–20,910. https://doi.org/10.1029/1998JC900099

De Steur, L., & Van Leeuwen, P. J. (2009). The influence of bottom topography on the decay of modeled Agulhas rings. *Deep Sea Research Part I: Oceanographic Research Papers*, *56*(4), 471–494. https://doi.org/10.1016/j.dsr.2008.11.009

Dencausse, G., Arhan, M., & Speich, S. (2010a). Routes of Agulhas rings in the southeastern Cape Basin. *Deep Sea Research Part I: Oceanographic Research Papers*, *57*(11), 1406–1421. https://doi.org/10.1016/j.dsr.2010.07.008

Dencausse, G., Arhan, M., & Speich, S. (2010b). Spatio-temporal characteristics of the Agulhas Current retroflection. *Deep Sea Research Part I: Oceanographic Research Papers*, *57*(11), 1392–1405. https://doi.org/10.1016/j.dsr.2010.07.004

Doglioli, A. M., Blanke, B., Speich, S., & Lapeyre, G. (2007). Tracking coherent structures in a regional ocean model with wavelet analysis: Application to Cape Basin eddies. *Journal of Geophysical Research*, *112*, C05043. https://doi.org/10.1029/2006JC003952

Dong, S., Garzoli, S., & Baringer, M. (2011). The role of interocean exchanges on decadal variations of the meridional heat transport in the South Atlantic. *Journal of Physical Oceanography*, *41*(8), 1498–1511. https://doi.org/10.1175/2011JPO4549.1

Donners, J., & Drijfhout, S. S. (2004). The Lagrangian view of South Atlantic interocean exchange in a global ocean model compared with inverse model results. *Journal of Physical Oceanography*, *34*(5), 1019–1035. https://doi.org/10.1175/1520-0485(2004)034<1019:TLVOSA>2.0.CO;2

Du, Y., Yi, J., Wu, D., He, Z., Wang, D., & Liang, F. (2014). Mesoscale oceanic eddies in the South China Sea from 1992 to 2012: Evolution processes and statistical analysis. *Acta Oceanologica Sinica*, *33*(11), 36–47. https://doi.org/10.1007/s13131-014-0530-6

Duacs/AVISO+ (2015). SSALTO/DUACS user handbook:(M) SLA and (M) ADT near-real time and delayed time products. CLS-DOS-NT-06-034 6, 74.

Duacs/AVISO+ (2017). Mesoscale eddy trajectory atlas product handbook. SALP-MU-P-EA-23126-CLS 17.

Duncombe Rae, C. (1991). Agulhas retroflection rings in the South Atlantic Ocean: An overview. *South African Journal of Marine Science*, *11*(1), 327–344. https://doi.org/10.2989/025776191784287574

Duncombe Rae, C., Garzoli, S., & Gordon, A. (1996). The eddy field of the southeast Atlantic Ocean: A statistical census from the Benguela Sources and Transports Project. *Journal of Geophysical Research*, *101*(C5), 11,949–11,964. https://doi.org/10.1029/95JC03360

Faghmous, J. H., Frenger, I., Yao, Y., Warmka, R., Lindell, A., & Kumar, V. (2015). A daily global mesoscale ocean eddy dataset from satellite altimetry. *Scientific Data*, *2*, 150028. https://doi.org/10.1038/sdata.2015.28

Ferrari, R., & Wunsch, C. (2009). Ocean circulation kinetic energy: Reservoirs, sources, and sinks. *Annual Review of Fluid Mechanics*, *41*, 253–282. https://doi.org/10.1146/annurev.fluid.40.111406.102139

Frenger, I., Gruber, N., Knutti, R., & Münnich, M. (2013). Imprint of Southern Ocean eddies on winds, clouds and rainfall. *Nature geoscience*, *6*(8), 608. https://doi.org/10.1038/ngeo1863

Garzoli, S. L., Richardson, P. L., Duncombe Rae, C. M., Fratantoni, D. M., Goñi, G. J., & Roubicek, A. J. (1999). Three Agulhas rings observed during the Benguela Current Experiment. *Journal of Geophysical Research*, *104*(C9), 20,971–20,985. https://doi.org/10.1029/1999JC900060

Gaube, P., Braun, C. D., Lawson, G. L., McGillicuddy, D. J., Della Penna, A., Skomal, G. B., & Thorrold, S. R. (2018). Mesoscale eddies influence the movements of mature female white sharks in the Gulf Stream and Sargasso Sea. *Scientific Reports*, *8*(1), 7363. https://doi.org/10.1038/s41598-018-25565-8

Gordon, A. L., & Haxby, W. F. (1990). Agulhas eddies invade the South Atlantic: Evidence from Geosat altimeter and shipboard conductivity-temperature-depth survey. *Journal of Geophysical Research*, *95*(C3), 3117–3125. https://doi.org/10.1029/JC095iC03p03117

Gordon, A. L., Weiss, R., Smethie, W., & Warner, M. (1992). Thermocline and intermediate water communication between the South Atlantic and Indian Oceans. *Journal of Geophysical Research*, *97*, 7223–7240. https://doi.org/10.1029/92JC00485

Gründlingh, M. L. (1995). Tracking eddies in the southeast Atlantic and southwest Indian oceans with TOPEX/POSEIDON. *Journal of Geophysical Research*, *100*(C12), 24,977–24,986. https://doi.org/10.1029/95JC01985

Guerra, L. A. A., Paiva, A. M., & Chassignet, E. P. (2018). On the translation of Agulhas rings to the western South Atlantic Ocean. *Deep Sea Research Part I: Oceanographic Research Papers*, *139*, 104–113. https://doi.org/10.1016/j.dsr.2018.08.005

Hausmann, U., & Czaja, A. (2012). The observed signature of mesoscale eddies in sea surface temperature and the associated heat transport. *Deep Sea Research Part I: Oceanographic Research Papers*, *70*, 60–72. https://doi.org/10.1016/j.dsr.2012.08.005

Herbette, S., Morel, Y., & Arhan, M. (2004). Subduction of a surface vortex under an outcropping front. *Journal of Physical Oceanography*, *34*(7), 1610–1627. https://doi.org/10.1175/1520-0485(2004)034<1610:SOASVU>2.0.CO;2

Holte, J., & Talley, L. (2009). A new algorithm for finding mixed layer depths with applications to Argo data and subantarctic mode water formation. *Journal of Atmospheric and Oceanic Technology*, *26*(9), 1920–1939. https://doi.org/10.1175/2009JTECHO543.1

Holte, J., Talley, L. D., Gilson, J., & Roemmich, D. (2017). An Argo mixed layer climatology and database. *Geophysical Research Letters*, *44*, 5618–5626. https://doi.org/10.1002/2017GL073426

Isern-Fontanet, J., García-Ladona, E., & Font, J. (2006). Vortices of the Mediterranean Sea: An altimetric perspective. *Journal of Physical Oceanography*, *36*(1), 87–103. https://doi.org/10.1175/JPO2826.1

Jayne, S. R., & Marotzke, J. (2002). The oceanic eddy heat transport. *Journal of Physical Oceanography*, *32*(12), 3328–3345. https://doi.org/10.1175/1520-0485(2002)032<3328:TOEHT>2.0.CO;2

Lampitt, R., Favali, P., Barnes, C., Church, M., Cronin, M., Hill, K., & Weller, R. (2010). In situ sustained Eulerian observatories. *Proceedings of the OceanObs*, *9*, 27. https://doi.org/10.5270/OceanObs09.pp.27

Laxenaire, R., Speich, S., Blanke, B., Chaigneau, A., Pegliasco, C., & Stegner, A. (2018). Anticyclonic eddies connecting the western boundaries of Indian and Atlantic Oceans. *Journal of Geophysical Research: Oceans*, *123*, 7651–7677. https://doi.org/10.1029/2018JC014270

Laxenaire, R., Speich, S., & Stegner, A. (2019). Evolution of the thermohaline structure of one Agulhas Ring reconstructed from satellite altimetry and Argo floats. *Journal of Geophysical Research: Oceans*, *124*, 8969–9003. https://doi.org/10.1029/2018JC014426

Le Vu, B., Stegner, A., & Arsouze, T. (2018). Angular Momentum Eddy Detection and tracking Algorithm (AMEDA) and its application to coastal eddy formation. *Journal of Atmospheric and Oceanic Technology*, *35*(4), 739–762. https://doi.org/10.1175/JTECH-D-17-0010.1

Lebedev, K. V., Yoshinari, H., Maximenko, N. A., & Hacker, P. W. (2007). Velocity data assessed from trajectories of Argo floats at parking level and at the sea surface. *IPRC Technical Note*, *4*(2), 1–16.

Li, Q.-Y., Sun, L., Liu, S.-S., Xian, T., & Yan, Y.-F. (2014). A new mononuclear eddy identification method with simple splitting strategies. *Remote Sensing Letters*, *5*(1), 65–72. https://doi.org/10.1080/2150704X.2013.872814

Locarnini, R., Mishonov, A., Baranova, O., Boyer, T., Zweng, M., Garcia, H., et al. (2019). World Ocean Atlas 2018, Volume 1: Temperature.

Lozier, M. S. (1997). Evidence for large-scale eddy-driven gyres in the North Atlantic. *Science*, *277*(5324), 361–364. https://doi.org/10.1126/science.277.5324.361

Lumpkin, R. (2016). Global characteristics of coherent vortices from surface drifter trajectories. *Journal of Geophysical Research: Oceans*, *121*, 1306–1321. https://doi.org/10.1002/2015JC011435

Lutjeharms, J. (2006). *The Agulhas current* (Vol. 5). Berlin: Springer-Verlag. https://doi.org/10.1007/3-540-37212-1

Lutjeharms, J., & Gordon, A. (1987). Shedding of an Agulhas ring observed at sea. *Nature*, *325*(6100), 138–140. https://doi.org/10.1038/325138a0

Mason, E., Pascual, A., & McWilliams, J. C. (2014). A new sea surface height-based code for oceanic mesoscale eddy tracking. *Journal of Atmospheric and Oceanic Technology*, *31*(5), 1181–1188. https://doi.org/10.1175/JTECH-D-14-00019.1

Matsuoka, D., Araki, F., Inoue, Y., & Sasaki, H. (2016). A new approach to ocean eddy detection, tracking, and event visualization–Application to the northwest Pacific Ocean. *Procedia Computer Science*, *80*, 1601–1611. https://doi.org/10.1016/j.procs.2016.05.491

McDonagh, E. L., Heywood, K. J., & Meredith, M. P. (1999). On the structure, paths, and fluxes associated with Agulhas rings. *Journal of Geophysical Research*, *104*(C9), 21,007–21,020. https://doi.org/10.1029/1998JC900131

McDougall, T. J., & Barker, P. M. (2011). Getting started with TEOS-10 and the Gibbs Seawater (GSW) oceanographic toolbox. *SCOR/IAPSO WG*, *127*, 1–28.

McGillicuddy, D. Jr., Johnson, R., Siegel, D., Michaels, A., Bates, N., & Knap, A. (1999). Mesoscale variations of biogeochemical properties in the Sargasso Sea. *Journal of Geophysical Research*, *104*(C6), 13,381–13,394. https://doi.org/10.1029/1999JC900021

McWilliams, J. C. (1985). Submesoscale, coherent vortices in the ocean. *Reviews of Geophysics*, *23*(2), 165–182. https://doi.org/10.1029/RG023i002p00165

Morrow, R., Coleman, R., Church, J., & Chelton, D. (1994). Surface eddy momentum flux and velocity variances in the Southern Ocean from Geosat altimetry. *Journal of Physical Oceanography*, *24*(10), 2050–2071. https://doi.org/10.1175/1520-0485(1994)024<2050:SEMFAV>2.0.CO;2

Morrow, R., & Le Traon, P.-Y. (2012). Recent advances in observing mesoscale ocean dynamics with satellite altimetry. *Advances in Space Research*, *50*(8), 1062–1076. https://doi.org/10.1016/j.asr.2011.09.033

Nan, F., Yu, F., Wei, C., Ren, Q., & Fan, C. (2017). Observations of an extra-large subsurface anticyclonic eddy in the northwestern Pacific subtropical gyre. *Journal of Marine Science: Research & Development*, *7*, 234. https://doi.org/10.4172/2155-9910.1000234

Nencioli, F., Dall'Olmo, G., & Quartly, G. D. (2018). Agulhas ring transport efficiency from combined satellite altimetry and Argo profiles. *Journal of Geophysical Research: Oceans*, *123*, 5874–5888. https://doi.org/10.1029/2018JC013909

Nencioli, F., Dong, C., Dickey, T., Washburn, L., & McWilliams, J. C. (2010). A vector geometry-based eddy detection algorithm and its application to a high-resolution numerical model product and high-frequency radar surface velocities in the Southern California Bight. *Journal of Atmospheric and Oceanic Technology*, *27*(3), 564–579. https://doi.org/10.1175/2009JTECHO725.1

Olson, D. B., & Evans, R. H. (1986). Rings of the Agulhas current. *Deep Sea Research Part A. Oceanographic Research Papers*, *33*(1), 27–42. https://doi.org/10.1016/0198-0149(86)90106-8

Owens, W. B., & Wong, A. P. (2009). An improved calibration method for the drift of the conductivity sensor on autonomous CTD profiling floats by θ-S climatology. *Deep Sea Research Part I: Oceanographic Research Papers*, *56*(3), 450–457. https://doi.org/10.1016/j.dsr.2008.09.008

Pegliasco, C., Chaigneau, A., & Morrow, R. (2015). Main eddy vertical structures observed in the four major Eastern Boundary Upwelling Systems. *Journal of Geophysical Research: Oceans*, *120*, 6008–6033. https://doi.org/10.1002/2015JC010950

Qiu-Yang, L., Sun, L., & Sheng-Fu, L. (2016). GEM: A dynamic tracking model for mesoscale eddies in the ocean. *Ocean Science*, *12*(6), 1249. https://doi.org/10.5194/os-12-1249-2016

Roemmich, D., & Gilson, J. (2001). Eddy transport of heat and thermocline waters in the North Pacific: A key to interannual/decadal climate variability? *Journal of Physical Oceanography*, *31*(3), 675–687. https://doi.org/10.1175/1520-0485(2001)031<0675:ETOHAT>2.0.CO;2

Sallée, J.-B., Speer, K., Rintoul, S., & Wijffels, S. (2010). Southern Ocean thermocline ventilation. *Journal of Physical Oceanography*, *40*(3), 509–529. https://doi.org/10.1175/2009JPO4291.1

Sánchez, R., & Gil, J. (2004). 3D structure, mesoscale interactions and potential vorticity conservation in a Swoddy in the Bay of Biscay. *Journal of Marine Systems*, *46*(1), 47–68. https://doi.org/10.1016/j.jmarsys.2003.10.002

Schmid, C., Boebel, O., Zenk, W., Lutjeharms, J., Garzoli, S., Richardson, P., & Barron, C. (2003). Early evolution of an Agulhas Ring. *Deep Sea Research Part II: Topical Studies in Oceanography*, *50*(1), 141–166. https://doi.org/10.1016/S0967-0645(02)00382-X

Schouten, M. W., de Ruijter, W. P. M., van Leeuwen, P. J., & Lutjeharms, J. R. E. (2000). Translation, decay and splitting of Agulhas rings in the southeastern Atlantic Ocean. *Journal of Geophysical Research*, *105*(C9), 21,913–21,925. https://doi.org/10.1029/1999JC000046

Schütte, F., Brandt, P., & Karstensen, J. (2016). Occurrence and characteristics of mesoscale eddies in the tropical northeast Atlantic Ocean. *Ocean Science*, *12*(3), 663–685. https://doi.org/10.5194/os-12-663-2016

Souza, J. M. A. C., de Boyer Montégut, C., Cabanes, C., & Klein, P. (2011). Estimation of the Agulhas ring impacts on meridional heat fluxes and transport using ARGO floats and satellite data. *Geophysical Research Letters*, *38*, L21602. https://doi.org/10.1029/2011GL049359

Stammer, D. (1997). Global characteristics of ocean variability estimated from regional TOPEX/POSEIDON altimeter measurements. *Journal of Physical Oceanography*, *27*(8), 1743–1769. https://doi.org/10.1175/1520-0485(1997)027<1743:GCOOVE>2.0.CO;2

Stammer, D., & Cazenave, A. (2017). *Satellite altimetry over oceans and land surfaces*. Boca Raton, FL, USA: CRC Press. https://doi.org/10.1201/9781315151779

Stammer, D., Hinrichsen, H.-H., & Käse, R. H. (1991). Can meddies be detected by satellite altimetry? *Journal of Geophysical Research*, *96*(C4), 7005–7014. https://doi.org/10.1029/90JC02740

Sweeney, E., McGillicuddy, D. Jr., & Buesseler, K. (2003). Biogeochemical impacts due to mesoscale eddy activity in the Sargasso Sea as measured at the Bermuda Atlantic Time-series Study (BATS). *Deep Sea Research Part II: Topical Studies in Oceanography*, *50*(22), 3017–3039. The US JGOFS Synthesis and Modeling Project: Phase II https://doi.org/10.1016/j.dsr2.2003.07.008

Van Aken, H., Van Veldhoven, A., Veth, C., De Ruijter, W., Van Leeuwen, P., Drijfhout, S., et al. (2003). Observations of a young Agulhas ring, Astrid, during MARE in March 2000. *Deep Sea Research Part II: Topical Studies in Oceanography*, *50*(1), 167–195. https://doi.org/10.1016/S0967-0645(02)00383-1

Walker, N. D. (1990). Links between South African summer rainfall and temperature variability of the Agulhas and Benguela Current systems. *Journal of Geophysical Research*, *95*(C3), 3297–3319. https://doi.org/10.1029/JC095iC03p03297

Walker, N. D., & Mey, R. D. (1988). Ocean/atmosphere heat fluxes within the Agulhas Retroflection region. *Journal of Geophysical Research*, *93*(C12), 15,473–15,483. https://doi.org/10.1029/JC093iC12p15473

Wang, Y., Beron-Vera, F., & Olascoaga, M. (2016). The life cycle of a coherent Lagrangian Agulhas ring. *Journal of Geophysical Research: Oceans*, *121*, 3944–3954. https://doi.org/10.1002/2015JC011620

Wang, Y., Olascoaga, M., & Beron-Vera, F. (2015). Coherent water transport across the South Atlantic. *Geophysical Research Letters*, *42*, 4072–4079. https://doi.org/10.1002/2015GL064089

Wang, Z.-F., Sun, L., Li, Q.-Y., & Cheng, H. (2019). Two typical merging events of oceanic mesoscale anticyclonic eddies. *Ocean Science*, *15*(6), 1545–1559. https://doi.org/10.5194/os-15-1545-2019

Wunsch, C. (1999). Where do ocean eddy heat fluxes matter? *Journal of Geophysical Research*, *104*(C6), 13,235–13,249. https://doi.org/10.1029/1999JC900062

Yang, G., Wang, F., Li, Y., & Lin, P. (2013). Mesoscale eddies in the northwestern subtropical Pacific Ocean: Statistical characteristics and three-dimensional structures. *Journal of Geophysical Research: Oceans*, *118*, 1906–1925. https://doi.org/10.1002/jgrc.20164

Yi, J., Du, Y., He, Z., & Zhou, C. (2014). Enhancing the accuracy of automatic eddy detection and the capability of recognizing the multi-core structures from maps of sea level anomaly. *Ocean Science*, *10*(1), 39. https://doi.org/10.5194/os-10-39-2014

Zhang, Z., Zhang, Y., & Wang, W. (2017). Three-compartment structure of subsurface-intensified mesoscale eddies in the ocean. *Journal of Geophysical Research: Oceans*, *122*, 1653–1664. https://doi.org/10.1002/2016JC012376

Zhang, Z., Zhang, Y., Wang, W., & Huang, R. X. (2013). Universal structure of mesoscale eddies in the ocean. *Geophysical Research Letters*, *40*, 3677–3681. https://doi.org/10.1002/grl.50736

Zweng, M., Reagan, J., Seidov, D., Boyer, T., Locarnini, R., Garcia, H., et al. (2019). World Ocean Atlas 2018, Volume 2: Salinity. In A. Mishonov Technical Ed.; NOAA Atlas NESDIS 82, 50 pp.